Minnesota Department of Transportation

RESEARCH SERVICES

Office of Policy Analysis, Research & Innovation

Mechanistic Modeling of Unbonded Concrete Overlay Pavements

Roberto Ballarini, Principal Investigator
Department of Civil Engineering
University of Minnesota

January 2012

Research Project
Final Report 2012-02

Your Destination...Our Priority

All agencies, departments, divisions and units that develop, use and/or purchase written materials for distribution to the public must ensure that each document contain a statement indicating that the information is available in alternative formats to individuals with disabilities upon request. Include the following statement on each document that is distributed:

To request this document in an alternative format, call Bruce Lattu at 651-366-4718 or 1-800-657-3774 (Greater Minnesota); 711 or 1-800-627-3529 (Minnesota Relay). You may also send an e-mail to bruce.lattu@state.mn.us. (Please request at least one week in advance).

Technical Report Documentation Page

1. Report No.	2.	3. Recipients Accession No.
MN/RC 2012-02		

4. Title and Subtitle	5. Report Date
Mechanistic Modeling of Unbonded Concrete Overlay Pavements	January 2012
	6.

7. Author(s)	8. Performing Organization Report No.
Roberto Ballarini, Minmao Liao	

9. Performing Organization Name and Address	10. Project/Task/Work Unit No.
University of Minnesota Department of Civil Engineering 500 Pillsbury Road Minneapolis, MN 55455	CTS Project #2010014
	11. Contract (C) or Grant (G) No. (c) 89261 (wo) 140

12. Sponsoring Organization Name and Address	13. Type of Report and Period Covered
Minnesota Department of Transportation Research Services Section 395 John Ireland Blvd., MS 330 St. Paul, MN 55155	Final Report
	14. Sponsoring Agency Code

15. Supplementary Notes
http://www.lrrb.org/pdf/201202.pdf

16. Abstract (Limit: 250 words)

An unbonded concrete overlay (UBCO) system is a Portland cement concrete (PCC) overlay that is separated from an existing PCC pavement by an asphalt concrete (AC) interlayer. Current UBCO design procedures are based on empirical equations or highly simplified mechanistic models. To overcome the limitations, fracture mechanics concepts, specifically the finite element method-based cohesive zone model (CZM), are introduced in this research as a new paradigm for analyzing UBCOs with the ultimate goal of establishing a more rational design procedure. To illustrate the advantages of a fracture mechanics-based approach to design, specific attention is paid to but one type of failure associated with pavement structures: reflection cracking. The design against reflection cracking approach relies on a load-carrying capacity equivalency between the designed UBCO and a reference newly designed single layer PCC pavement.

An illustrative fracture mechanics-based design procedure for UBCOs is developed and proposed by a large number of crack propagation simulations of both the UBCO composite and the reference single layer pavement. Preliminary comparisons of the results with field observations suggest that the fracture mechanics paradigm offers promise for improved design of UBCOs against reflection cracking and other potential loading conditions that could be analyzed using nonlinear fracture mechanics models.

It is recommended that an experimental program be established to assess the accuracy of the model predictions, and additional experiments and three-dimensional fracture mechanics simulations be considered to provide additional insights as to whether UBCOs can be “thinned-up”.

17. Document Analysis/Descriptors	18. Availability Statement
Overlays (Pavements), Composite structures, Cracking, Fracture mechanics, Finite element method, Traffic equivalence factor	No restrictions. Document available from: National Technical Information Services, Alexandria, Virginia 22312

19. Security Class (this report)	20. Security Class (this page)	21. No. of Pages	22. Price
		79	

Mechanistic Modeling of Unbonded Concrete Overlay Pavements

Final Report

Prepared by:

Roberto Ballarini
Minmao Liao

Department of Civil Engineering
University of Minnesota

January 2012

Published by:

Minnesota Department of Transportation
Research Services Section
395 John Ireland Boulevard, Mail Stop 330
St. Paul, Minnesota 55155

This report represents the results of research conducted by the authors and does not necessarily represent the views or policies of the Minnesota Department of Transportation or the University of Minnesota. This report does not contain a standard or specified technique.

The authors, the Minnesota Department of Transportation, and the University of Minnesota do not endorse products or manufacturers. Any trade or manufacturers' names that may appear herein do so solely because they are considered essential to this report.

ACKNOWLEDGMENTS

The authors acknowledge support from the Minnesota Department of Transportation and the James L. Record Chair and discussions with Dr. Lev Khazanovich. Computing resources were provided by the Minnesota Supercomputing Institute.

TABLE OF CONTENTS

1 INTRODUCTION 1
1.1 Background 1
1.2 Problem Statement 2
1.3 Research Methodology 5
1.4 Research Objectives 6
1.5 Report Organization 6
2 LITERATURE REVIEW AND FRACTURE MECHANICS CONCEPTS 8
2.1 Minnesota's UBCO Design Procedures 8
2.1.1 COE Procedure 8
2.1.2 PCA Procedure 9
2.2 Fracture Mechanics 11
2.2.1 Linear Elastic Fracture Mechanics 13
2.2.2 Nonlinear Fracture Mechanics 15
2.2.3 CZMs for Concrete and Asphalt 18
2.2.4 Application of CZMs in Pavement Engineering 20
2.3 Summary 21
3 MODELING VERIFICATION 22
3.1 Introduction 22
3.2 Infinite Plate with Circular Hole under Uniaxial Tension 22
3.3 Notched Concrete Beam under Three-Point Bending 25
3.4 Summary 27
4 SINGLE-LAYER PCC PAVEMENT 28
4.1 Introduction 28
4.2 Finite Element Model 28
4.3 Normalized Load Capacity 30
4.4 Summary 33
5 UNBONDED CONCRETE OVERLAY PAVEMENT 34
5.1 Introduction 34
5.2 Finite Element Model 34
5.3 Structural Equivalency Design 40
5.4 Summary 41
6 FIELD STUDY 42
6.1 Introduction 42

6.2 Field Study 42
6.3 Summary 43
7 CONCLUSIONS AND RECOMMENDATIONS 44
REFERENCES 45
APPENDIX A: MNDOT UBCO DESIGN PROCEDURE
APPENDIX B: COHESIVE ELEMENTS IN ABAQUS
APPENDIX C: BEAMS ON ELASTIC FOUNDATIONS
APPENDIX D: DAKOTA
APPENDIX E: SIMULATION RESULTS

LIST OF FIGURES

Figure 1.1. Schematic of an UBCO system 1
Figure 1.2. Proposed structurally equivalent structures 6
Figure 2.1. Concept of stress equivalency (from Tayabji and Okamoto, 1985) 9
Figure 2.2. UBCO design charts (from Tayabji and Okamoto, 1985) 10
Figure 2.3. Stress concentrations caused by a circular hole, an elliptical cavity and a crack in an infinite plate subjected to uniform tension 12
Figure 2.4. Definition of coordinate systems at a point along a crack front 13
Figure 2.5. Schematic of stress field within and ahead of a process zone 14
Figure 2.6. Dugdale model 16
Figure 2.7. Transition between ductile and brittle response of a cracked structure 17
Figure 2.8. Cohesive zone model 18
Figure 2.9. Bilinear softening cohesive law 19
Figure 3.1. Mesh of a plate containing a circular hole and a cohesive zone 22
Figure 3.2. Normalized strength versus normalized structural size 23
Figure 3.3. Tensile stress distributions along the cohesive zone 24
Figure 3.4. Development of principal tensile stresses along the cohesive zone 25
Figure 3.5. Finite element mesh of the concrete beam 26
Figure 3.6. Approximate stress-crack opening displacement curves of concrete 26
Figure 3.7. Load versus CMOD 27
Figure 4.1. Cohesive zone model of a single-layer PCC pavement 28
Figure 4.2. Bilinear traction-separation relationship of concrete 29
Figure 4.3. Deformation and tensile stress distribution along the cohesive zone 30
Figure 4.4. Φ versus L/l 32
Figure 4.5. Normalized load capacity versus h/l_{ch} 33
Figure 5.1. Cohesive zone model of an UBCO system 34
Figure 5.2. Illustrative crack initiation and propagation 35
Figure 5.3. Derived relationship between the capacity and the variables 38
Figure 6.1. MnROAD test sections of UBCOs 42

LIST OF TABLES

Table 1.1. Design factors considered by UBCO design procedures (from ERES, 1999) 3
Table 2.1. MnDOT required minimum thickness of UBCOs (in inches) 8

EXECUTIVE SUMMARY

An unbonded concrete overlay (UBCO) system is a Portland cement concrete (PCC) overlay that is separated from an existing PCC pavement by an asphalt concrete (AC) interlayer. It is an increasingly popular method for highway pavement rehabilitation. However, current UBCO design procedures are based on empirical equations or highly simplified mechanistic models.

To overcome the limitations, fracture mechanics concepts, specifically the finite element method-based cohesive zone model (CZM), are introduced in this research as a new paradigm for analyzing UBCOs with the ultimate goal of establishing a more rational design procedure. Pavements can fail as a result of a wide variety of loadings, including thermal and mechanical. Furthermore, the failures can be produced by different forms of cracking, be it of the fast or the fatigue types. To illustrate the advantages of a fracture mechanics-based approach to design, specific attention is paid to but one type of failure associated with pavement structures: reflection cracking. The design against reflection cracking approach relies on a load-carrying capacity equivalency between the designed UBCO and a reference, newly designed, single-layer PCC pavement.

The research begins with the two-dimensional analysis of the single-layer pavement. A dimensionless equation relating the pavement's load capacity to its material properties and geometric dimensions is obtained from the results of a large number of failure simulations. The single-layer exercise is followed by a three-layer model that includes the dimensions and material properties of the overlay and the interlayer, wherein a preexisting crack exists in the existing PCC pavement.

A fracture mechanics-based design procedure for UBCOs is developed and proposed by a large number of crack propagation simulations of both the UBCO composite and the reference single-layer pavement. Preliminary comparisons of the results with field observations suggest that the fracture mechanics paradigm offers promise for improved design of UBCOs against reflection cracking and other potential loading conditions that could be analyzed using nonlinear fracture mechanics models.

It is recommended that an experimental program be established to assess the accuracy of the model predictions, and additional experiments and three-dimensional fracture mechanics simulations be considered to provide additional insights as to whether UBCOs can be "thinned-up".

1 INTRODUCTION

1.1 Background

Large increases in traffic and the end of the service life of a significant number of existing pavements in the United States have produced growing demand for highway pavement rehabilitation. Among various rehabilitation techniques, unbonded concrete overlays (UBCOs) are likely to become increasingly popular because numerous states, such as Minnesota, Michigan, and Illinois, have found that they perform well when properly designed (Engstrom, 1993; Heckel, 2002). UBCOs are cost-effective and durable, mitigate reflection cracking, require minimal pre-overlay preparation, can be placed quickly and efficiently, and are recyclable. UBCOs have been used since the 1910s (ERES, 1999) to restore ride quality, provide an appropriate surface texture, restore or increase load-carrying capacity, and extend life of existing pavements.

A schematic of the UBCO system, as shown in Figure 1.1, consists of the existing damaged Portland cement concrete (PCC) pavement, a thin asphalt concrete (AC) interlayer, and a new PCC overlay. The 1 to 2-inch-thick (2.54 to 5.08-cm-thick) AC interlayer can be either newly constructed or preexisting. It is assumed (but has not been demonstrated) that it allows relative deformation between the overlay and the existing pavement, and serves to prevent the reflection cracking of the overlay that is associated with bonded concrete overlays (BCOs). Consequently, UBCOs can be used for badly damaged existing pavements, therefore minimizing pre-overlay repairs and reducing construction costs. An additional advantage of UBCOs in applications involving severely damaged foundations is that (unlike BCOs) their joints are not required to line up with those of the existing pavement. In fact, specific joint mismatching is usually recommended to provide a sleeper slab arrangement which improves load transfer. Finally, UBCOs can be used under any traffic level and climate scenario.

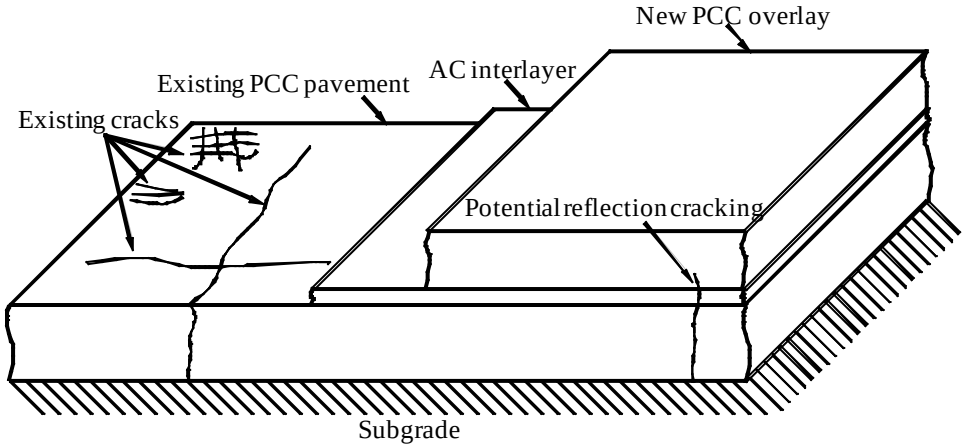

Figure 1.1. Schematic of an UBCO system

Construction of UBCOs is similar to that of conventional PCC pavements and does not require specialized equipment. However, special attention should be drawn to geometric constraints such as overhead vertical clearances. According to Minnesota's experience (Engstrom, 1993), compared to $500,000 for reconstructed PCC pavements, UBCOs cost only around $350,000 per

two lanes per mile. Therefore, with the advances in paving materials and paving technology, UBCOs are becoming more attractive as an alternative for highway pavement rehabilitation.

1.2 Problem Statement

Despite the advantages and numerous positive experiences summarized above, application of UBCOs is still limited to a few states. The main reason is that although several design procedures are currently available, none have been universally accepted. Hutchinson (1982), Smith et al. (1986), and Hall et al. (1993) summarized the assumptions and the limitations of UBCO design procedures available up to the mid-1990s.

ERES (1999) made a comprehensive review and evaluation of existing UBCO design procedures. Six main approaches were compared. Other procedures were closely associated with one of these approaches. Design factors considered by each approach are tabulated in Table 1.1 (from ERES, 1999). The table indicates that these approaches did not all consider the same design factors, and they employed different ways to consider the same factor. Finally, based on an analysis of a large amount of field performance data, guidelines for design and construction of UBCOs were proposed.

More recently, ERES (2004) developed a new pavement design guide based on mechanistic-empirical principles. The approach involves the selection of a trial design selected on the basis of site and construction conditions, and then the evaluation of the design using software M-E PDG Version 1.1 (ARA and ASU, 2009). The software creates simple finite element method models and applies Miner's cumulative damage rule (Miner, 1945) to evaluate the pavement's lifetime. If the trial design does not satisfy the requirements for future traffic, it is revised and the evaluation process is repeated as necessary.

The Innovative Pavement Research Foundation (IPRF) planned and conducted a series of experiments (Khazanovich, 2001; Stoffels, 2008, 2010) to identify key parameters to improve UBCO designs. However, the experiments were conducted on airfield pavements which experience loading conditions that are qualitatively and quantitatively different from those of highway pavements. In fact, the design procedures used for UBCOs for highway pavements have mirrored those developed for airfield pavements that are subjected to heavier but less frequent traffic loading cycles. The concern is that current highway pavement designs may require overly conservative overlay thicknesses and thus reduce cost-effectiveness. Therefore, this research may provide a potential opportunity to "thin-up" UBCO pavement systems, in turn reducing the construction cost and reducing the carbon footprint associated with production of concrete and cement. Many lay people are not aware and thus do not appreciate the environmental impact of the production of infrastructure materials. If one considers that hundreds of thousands of miles of highways will be built or rehabilitated in the 21st century, it makes good economic and environmental sense to reduce the design thickness of pavements.

Table 1.1. Design factors considered by UBCO design procedures (from ERES, 1999)

Design Factors	AASHTO (1993)	Corps of Engineers (Departments of the Army, and the Air Force, 1970)	Rollings (1988)
Analytical model	Empirical equation	Empirical equation	Layered elastic theory
Failure criteria	Deterioration in terms of serviceability loss	Cracking in 50%	Deterioration in terms of a structural condition index
Interface condition	Considers overlay to be fully unbonded	Power in design equation is adjusted to account for level of bonding	Varies between full bonding and completely unbonded
Material properties	Modulus of elasticity and flexural strength for overlay concrete, k-value for subgrade	Equivalent required thickness as input to empirical equation	Modulus of elasticity and Poisson's ratio for all materials, and flexural strength of overlay concrete
Difference in strength/modulus of overlay and base pavement concrete	Not considered	Thickness of base pavement is adjusted	Included directly in calculation of stresses and design factors
Cracking in base pavement before overlay	Effective thickness of base pavement is reduced	Effective thickness of base pavement is reduced	Modulus of elasticity of base pavement is reduced
Fatigue effects of traffic on uncracked existing pavement	Effective thickness of base pavement is reduced	Effective thickness of base pavement is reduced	Included in terms of equivalent traffic
Cracking of base after overlay	Not directly considered	Not directly considered	Modulus of elasticity of base is reduced to compensate for cracking under traffic
Temperature curling or moisture warping	Assumes AASHTO Road Test conditions	Not considered	Not considered
Joint spacing	Maximum joint spacing 1.75×overlay thickness	No recommendation provided	No recommendation provided
Joint load transfer	Thickness increased if not doweled	Dowels assumed	Not considered
Drainage	Included in thickness design by empirical coefficient	Not considered	Requires retrofit of drainage system (if necessary)
Interlayer	Recommends 1-inch minimum thick AC interlayer or permeable open-graded interlayer	No recommendation provided	No recommendation provided

Table 1.1. (continued) Design factors considered by UBCO design procedures

Design Factors	Portland Cement Association (Tayabji and Okamoto, 1985)	Belgium (Veverka, 1986)	MnDOT (1993)
Analytical model	Plate theory/finite element	Empirical equation	Corps of Engineers/Portland Cement Association
Failure criteria	Depends on failure criterion for full depth concrete design procedure	Fatigue failure; subgrade failure	Not applicable
Interface condition	Unbonded	Power in design equation is adjusted to account for level of bonding	Power in design equation is adjusted to account for level of bonding
Material properties	Modulus of elasticity and modulus of rupture for overlay concrete, k-value for subgrade	Modulus of elasticity for all layers	Modulus of elasticity and modulus of rupture for overlay concrete, k-value for subgrade
Difference in strength/modulus of overlay and base pavement concrete	Included directly in calculation of stresses and design factors	Not considered	Not considered
Cracking in base pavement before overlay	Included directly in calculation of stresses using soft elements	Thickness of base pavement is reduced	Thickness of base pavement is reduced
Fatigue effects of traffic on uncracked existing pavement	Not considered	Not considered	Not considered
Cracking of base after overlay	Not considered	Not considered	Not considered
Temperature curling or moisture warping	Does not affect thickness selection	Not considered	Not considered
Joint spacing	Maximum joint spacing 1.75×overlay thickness	Maximum joint spacing 18 feet	15 feet if 7 inches < overlay thickness < 10.5 inches; 20 feet if overlay thickness > 10.5 inches
Joint load transfer	Not specified for overlay but considered in evaluation of base pavement	Can be doweled or undoweled	Dowels assumed
Drainage	Edge drains are recommended where pumping and erosion has occurred in the existing slab	Not available	Edge drains and permeable interlayer for all pavements, interceptor drains when overlay is wider than the base pavement
Interlayer	Thin interlayer (<0.5 inch) if extensive repair work performed, thick (>0.5 inch) otherwise	Not available	> 1 inch > 2 inches if base pavement is badly faulted and/or has a rough profile

One example of current design procedures for UBCOs that are based on either empirical equations or highly simplified mechanistic models is the approach adopted by the Minnesota Department of Transportation (MnDOT, 1993). The procedure relies on empirical methods of Corps of Engineers (COE) developed by the Departments of the Army, and the Air Force (1970) and mechanistic models of Portland Cement Association (PCA) proposed by Tayabji and Okamoto (1985) which will be reviewed in detail in the next chapter. The former procedure is limited by its empirical nature, and the latter procedure's mechanistic models only consider a two-layer pavement system that neglects the AC interlayer, the accompanying interactions, and the fundamental material properties that influence crack initiation and propagation within the constituents. In addition, the mechanistic models employ traditional stress-based failure criteria within finite element method programs that cannot properly account for the stress singularities associated with geometric discontinuities such as preexisting cracks in the existing PCC pavement. Note that the mechanistic models created in the software M-E PDG Version 1.1 have such limitations.

1.3 Research Methodology

To overcome the limitations of design procedures that rely on stress-based failure criteria, this research introduces for the first time a nonlinear fracture mechanics paradigm for the design of UBCOs against reflection cracking. It is noted that other types of failures associated with the initiation and propagation of discrete cracks could be addressed using the procedures developed in this research. Specifically, the Cohesive Zone (or Fictitious Crack) Model (CZM) proposed for concrete (and other quasi-brittle materials) by Hillerborg et al. (1976) is employed in the analysis of the crack propagation that leads to pavement failure. The simulations performed in this research rely on the implementation of CZMs in the general purpose finite element code ABAQUS Version 6.10 (SIMULIA, 2010).

Because pavement engineers have developed relatively robust design procedures for new PCC pavements, including new single-layer pavements consisting of a PCC slab on a foundation, the structural equivalency design paradigm has been proposed to design UBCOs. A similar approach is adopted here. This procedure demands that the thickness of the UBCO be such that it attains the same value of a certain metric as does a single-layer pavement designed for the same service conditions. Some of the currently available mechanistic designs, including the Tayabji and Okamoto procedure, use stress equivalency; the maximum nominal stress in the UBCO and the single-layer pavement should be equal. However, as previously stated such stress-based material failure theories are not capable of quantifying the loads required to initiate and propagate the reflection cracks that emanate from singular stress-producing crack-like features in the existing PCC pavement. This research focuses precisely on this type of potential pavement failure through a two-dimensional CZM that relates the ultimate load capacity of the UBCO structure to fundamental material properties and geometric dimensions, captures the well-known size effect in quasi-brittle materials, and eliminates the mesh size-dependence that is present in existing stress-based mechanistic models.

The metric chosen here for structural equivalency is not a nominal stress within the pavement, but the maximum load achieved during the failure simulation of the two structures shown in Figure 1.2. The first represents a single-layer pavement resting on a foundation that under the action of a monotonically increasing point force experiences the initiation and propagation of a

crack at the location of maximum nominal stress in the initially uncracked configuration. The second is a three-layer UBCO system that under similar loading fails as a result of a reflection crack that forms at the tip of a crack-like feature representing a preexisting crack or joint in the existing pavement. The load capacities of both structures are determined from the results of the CZM. The UBCO and the single layer are deemed structurally equivalent if they have equal load capacity. Consequently, the proposed thickness design procedure for an UBCO is as follows. For the prescribed service requirements, a new single-layer PCC pavement is designed according to currently available robust procedures. The ultimate load capacity of the design is determined from a CZM failure simulation. The thickness and/or material properties of the UBCO are in turn determined to render it structurally equivalent to the single-layer configuration. As explained subsequently, the fracture mechanics approach accounts not only for the geometry, stiffness, and strength but also the fracture energy of each layer that comprises the UBCO pavement.

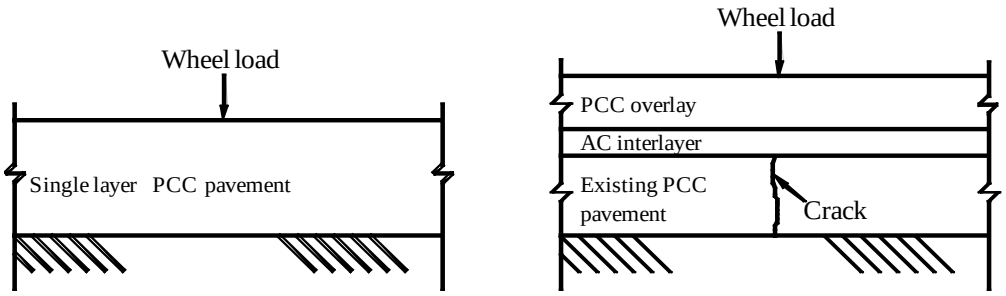

Figure 1.2. Proposed structurally equivalent structures

1.4 Research Objectives

According to the research methodology discussed above, the primary objectives of this research are as follows:

- To review existing design procedures for UBCOs adopted by MnDOT and to identify their limitations.
- To apply the CZM to pavement analysis and design using the finite element method.
- To examine the relationships between the ultimate load capacity, the material properties, and the geometry for both single-layer pavements and UBCOs.
- To develop, from the results of a large number of parameter studies, insights that could eventually lead to improved design procedures for UBCOs.
- To provide suggestions for future research.

1.5 Report Organization

The remaining part of this report is divided into the following six chapters.

Chapter 2 serves as a literature review that briefly summarizes and highlights the limitations of the design procedures for UBCOs currently used by MnDOT. In addition, the fundamental concepts of linear elastic fracture mechanics and the CZM are reviewed. The ability of fracture

mechanics to capture the dependence on absolute size of the nominal strength of geometrically similar structures (the so called size effect) is emphasized.

Chapter 3 verifies the ABAQUS finite element modeling of the CZM through two examples; an infinite plate with circular hole under uniaxial tension and a notched concrete beam under three-point bending. The simulation results are in turn compared to available theoretical or experimental data.

Chapter 4 presents the results of the failure simulations of the single-layer PCC pavement. The results of a large amount of simulations are used to derive an equation that relates the load-carrying capacity of this reference structure to fundamental material properties and structural dimensions.

Chapter 5 presents the results of similar simulations and load-carrying capacity formulas for UBCO pavements. Based on the load-carrying capacity equations obtained from Chapters 4 and 5, an illustrative design procedure for UBCOs produced from the structural equivalency concept is derived, and implications of the procedure are discussed. Specific attention is paid to the relative influence of all control variables on the load-carrying capacity and required overlay thickness.

Chapter 6 compares the implications of the proposed procedure with observations of UBCOs tested at the MnROAD test facility in Minnesota. The comparison suggests that currently available design procedures may indeed require conservative overlay thicknesses, and additional experiments and three-dimensional fracture mechanics simulations may provide additional insights as to whether UBCOs can be “thinned-up”.

Chapter 7 summarizes the main findings of the research and provides conclusions and recommendations.

2 LITERATURE REVIEW AND FRACTURE MECHANICS CONCEPTS

2.1 Minnesota's UBCO Design Procedures

MnDOT (1993) chooses the thickness of the overlay in an UBCO pavement as the average of the thicknesses dictated by two procedures (reviewed in Appendix A); the Corps of Engineers (COE) approach developed by the Departments of the Army, and the Air Force (1970), and the Portland Cement Association (PCA) method developed by Tayabji and Okamoto (1985). The design concept is based on providing a PCC overlay such that the existing PCC pavement plus the PCC overlay is structurally equivalent to a new single-layer PCC pavement designed to carry the estimated future traffic. The Minnesota procedure also specifies the required minimum thickness of the UBCO which depends on the widths of the PCC overlay and the existing PCC pavement, as listed in Table 2.1.

Table 2.1. MnDOT required minimum thickness of UBCOs (in inches)

		Overlay Width (feet)	
		27	24
Existing Pavement Width (feet)	27	6	*
	24	7	6
	22	*	7 **
	20	*	*

* Not appropriate design

** Unless recommended otherwise by MR&E's Pavement Engineering Section

2.1.1 COE Procedure

The COE procedure is based on an empirical equation that requires the PCC overlay to satisfy a structural deficiency between the required thickness for a new single-layer PCC pavement resting on the same subgrade and the thickness of the existing PCC pavement. The design equation is

$$h_o = \sqrt{h_n^2 - Ch_e^2} \tag{2.1}$$

where h_o is the required PCC overlay thickness, h_n is the thickness that would be required for a new single-layer PCC pavement resting on the same subgrade, h_e is the thickness of the existing PCC pavement, and C is a constant that depends on the condition of the existing PCC pavement. Recommended values for C are: 1.00 when the existing pavement is in good condition with little or no structural cracking; 0.75 when existing pavement has a few initial structural cracking but no progressive cracking; and 0.35 when existing pavement is badly cracked.

The empirical nature of the COE procedure immediately makes its application to a wide range of pavement materials and structural dimensions suspect. Perhaps the most obvious limitation of the equation is that it totally neglects the influence of the material properties of the constituent materials. For example, the equation neglects the influence of the dimensions and material

properties of the AC interlayer which will be shown in this research to be significant. In addition, the procedure was originally established for airfield pavements, whose traffic conditions are significantly different from those experienced by highway pavements. Therefore, its application to highway pavements is questionable.

2.1.2 PCA Procedure

The PCA procedure is based on finite element method-based mechanistic models. The existing PCC pavement and the PCC overlay are treated as distinct slabs resting on the subgrade. The analysis is conducted for the following conditions: 20-foot-long (6.1-m-long) joint spacing of overlays, 18,000 lb (80 kN) single axle load, 5,000 ksi (34.5 GPa) of the overlay's Young's modulus, 3,000 to 4,000 ksi (20.7 to 27.6 GPa) of the existing pavement's Young's modulus, and 100 to 300 pci (27.14 to 81.43 MPa/m) of the foundation stiffness. The procedure is based on a stress equivalency concept as illustrated in Figure 2.1. The design demands that the critical stress that develops in the PCC overlay is no larger than the stress that would be acceptable in a new single-layer PCC pavement resting on the same subgrade. Finally, the procedure presents three design charts as shown in Figure 2.2, which determine the PCC overlay thickness for three cases: (a) the existing pavement exhibits a large amount of midslab and corner cracking with poor load transfer at joints and cracks; (b) the existing pavement exhibits a small amount of midslab and corner cracking with reasonably good load transfer at joints and cracks; and (c) the existing pavement exhibits a small amount of midslab cracking with good load transfer at joints and cracks.

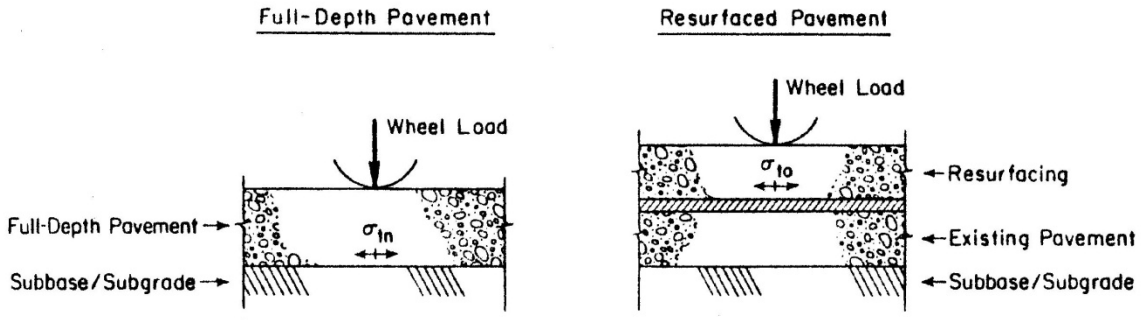

Figure 2.1. Concept of stress equivalency (from Tayabji and Okamoto, 1985)

The PCA procedure does not consider the presence of the AC interlayer. This is a major limitation because the interactions between the PCC overlay and the AC interlayer and between the existing PCC pavement and the AC interlayer will be shown in this research to be very significant. In addition, the model assumes a stress-based failure condition that cannot account properly for geometric discontinuities, and thus cannot be used to determine the load-carrying capacity associated with the initiation and propagation of cracks from preexisting cracks and joints. Therefore, this research introduces for the first time fracture mechanics that is capable of accounting for geometric discontinuities for UBCO designs against reflection cracking. Related fracture mechanics concepts and their application to pavement engineering are summarized in the next section.

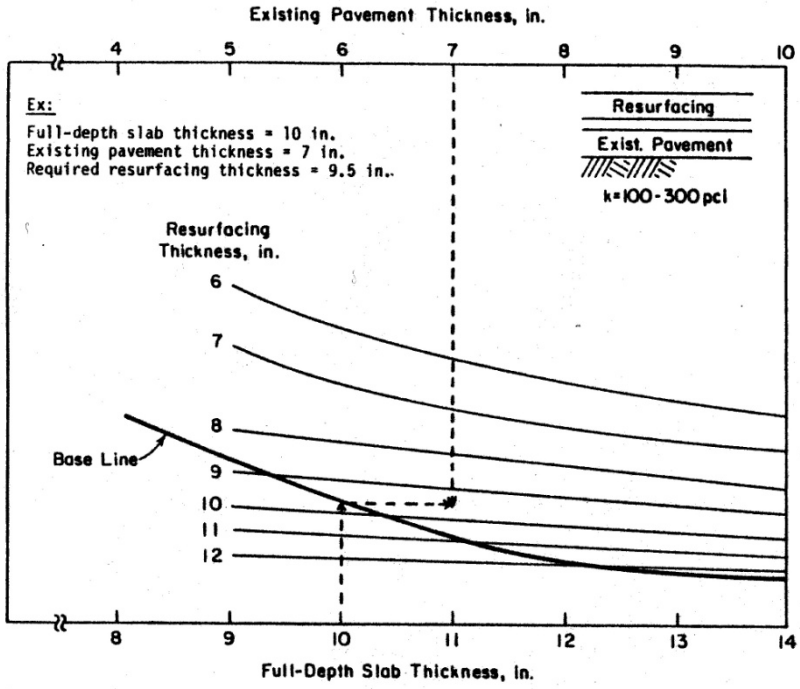

Case (a)

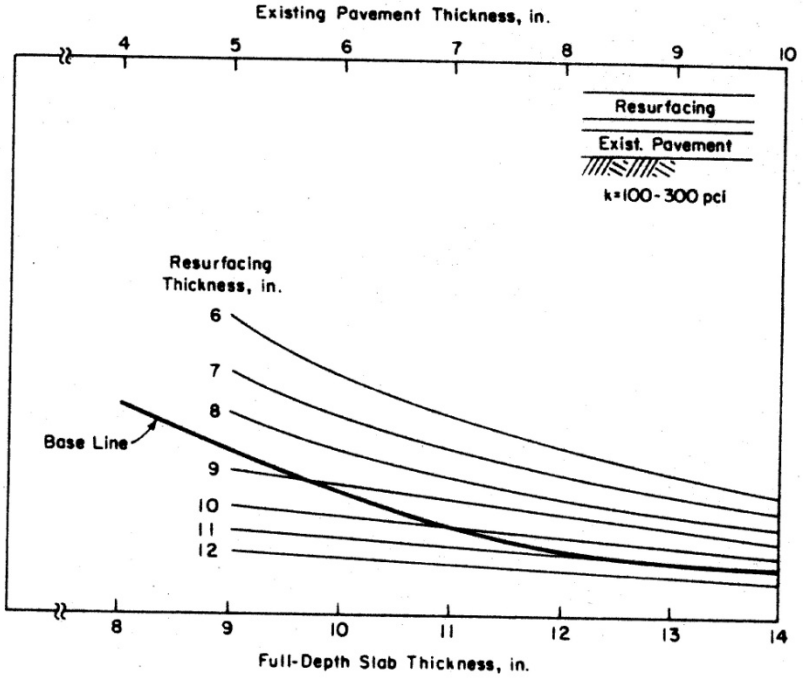

Case (b)

Figure 2.2. UBCO design charts (from Tayabji and Okamoto, 1985)

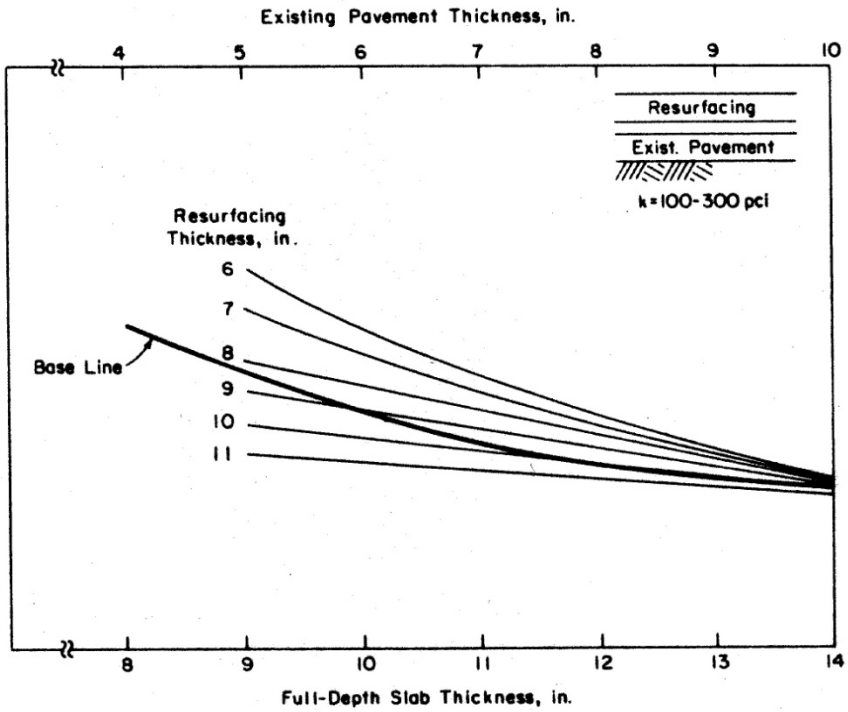

Case (c)

Figure 2.2. (continued) UBCO design charts (from Tayabji and Okamoto, 1985)

2.2 Fracture Mechanics

The initiation and growth of a crack (or any other type of geometric discontinuity) within a structure leads to stress redistribution within the material and stress concentration in the vicinity of the introduced "flaw". Consider, for example, an infinite plate made of linear elastic material subjected to a far-field uniform tensile stress $\sigma_{yy}^{\infty} = \sigma^{\infty}$ (Figure 2.3). The stress state produced by this loading is uniform, with $\sigma_{yy} = \sigma^{\infty}$ and all other stress components equal to zero. If the plate contains a circular hole of radius R, the state of stress in the vicinity of the hole is complex, and the maximum hoop stress at edge of the hole is $\sigma_{yy}(x = R,\ y = 0) = 3\sigma^{\infty}$; the Stress Concentration Factor (SCF) is equal to 3.0. If the circular hole is replaced by an elliptical cavity with major (minor) axis $2a$ ($2b$), then $\sigma_{yy}(x = a,\ y = 0) = \left(1 + \frac{2a}{b}\right)\sigma^{\infty}$. For this case the SCF increases with increasing aspect ratio, a / b, and becomes unbounded when the elliptical cavity approaches the shape of a sharp crack ($b / a \to 0$).

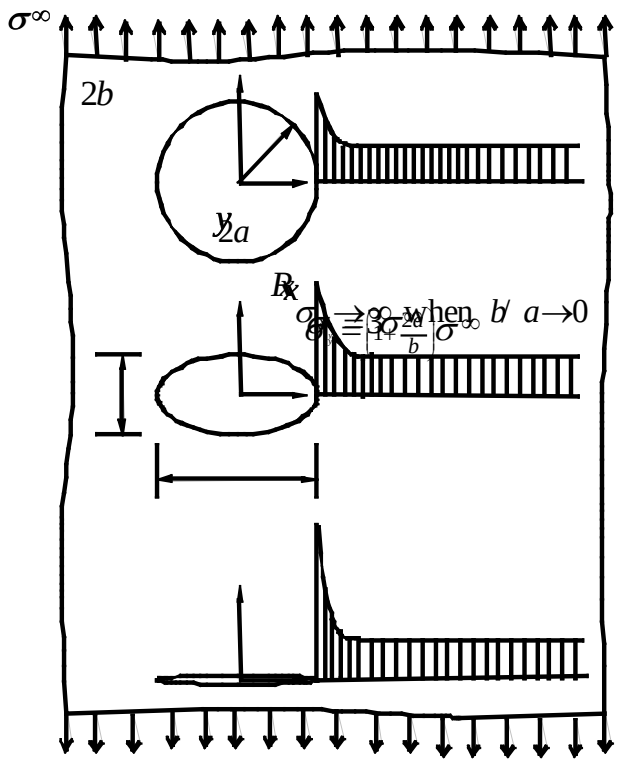

Figure 2.3. Stress concentrations caused by a circular hole, an elliptical cavity and a crack in an infinite plate subjected to uniform tension

Classical stress-based failure criteria have been and continue to be used to predict the load capacity (or fatigue life for cases of applied cyclic stress) of structures that are associated with finite SCFs. In such "strength theories", a combination of stresses or strains (referred to as the loading function) is computed through an analysis, and the damage is assumed to initiate and continue to grow when the loading function becomes equal to a critical value inferred by experimental data (the yield function). Obviously, stress-based approaches break down when the structure contains a crack and any combination of stresses at the crack front become infinite (infinite stresses are referred to as "singular"). This is certainly the case when a pavement develops a crack or contains a sharp joint. Linear elastic fracture mechanics (LEFM) is an energy-based theory that enables the use of the "pathological" behavior of the stress field to characterize crack initiation and growth.

In addition, it is emphasized that the use of strength models for quasi-brittle materials is problematic because nominal strength exhibits a relatively strong size effect. The nominal strength of a pavement depends on the thickness of the pavement. One of the advantages of nonlinear fracture mechanics (NLFM) is its ability to predict the size effect.

In the following first two sections we provide a brief summary of the stress intensity factor (SIF), energy release rate (ERR), and cohesive zone approaches to fracture mechanics. The first two are complementary and equivalent for cases involving purely brittle materials with relatively small damage zones near the crack front, and the third is an approach capable of predicting the load capacity of materials ranging from those that are very brittle to those that are capable of

significant large but localized damage ahead of the crack. Additional details of CZMs for concrete and asphalt and their use in pavement analyses are presented subsequently.

2.2.1 Linear Elastic Fracture Mechanics

Even though it was developed after the ERR approach, we present first the fracture toughness approach for predicting crack extension. Figure 2.4 is a close-up view of the vicinity of a crack front. The position of a material point is defined in terms of the polar coordinates r and θ in a coordinate system normal to the crack front, and coordinate z parallel to the front. Through the solution of the elasticity boundary value problem, it has been established that the stress and displacement fields very close to the crack front approach the "universal" form:

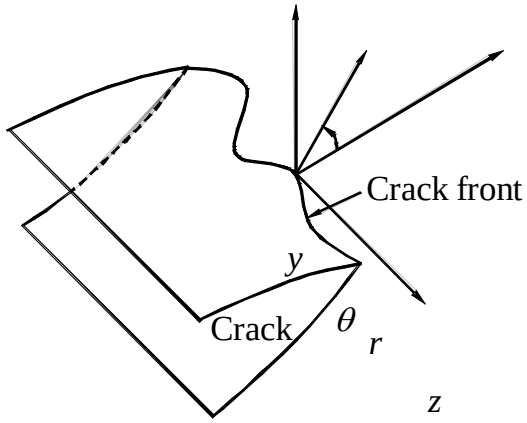

Figure 2.4. Definition of coordinate systems at a point along a crack front

$$\sigma_{xx} = \frac{K_I}{\sqrt{2\pi r}}\cos\frac{\theta}{2}\left(1-\sin\frac{\theta}{2}\sin\frac{3\theta}{2}\right) - \frac{K_{II}}{\sqrt{2\pi r}}\sin\frac{\theta}{2}\left(2+\cos\frac{\theta}{2}\cos\frac{3\theta}{2}\right)$$

$$\sigma_{yy} = \frac{K_I}{\sqrt{2\pi r}}\cos\frac{\theta}{2}\left(1+\sin\frac{\theta}{2}\sin\frac{3\theta}{2}\right) + \frac{K_{II}}{\sqrt{2\pi r}}\sin\frac{\theta}{2}\cos\frac{\theta}{2}\cos\frac{3\theta}{2}$$

$\sigma_{zz} = 0$ for plane stress ($\sigma_{zz} = \nu(\sigma_{xx} + \sigma_{yy})$ for plane strain)

$$\tau_{xy} = \frac{K_I}{\sqrt{2\pi r}}\sin\frac{\theta}{2}\cos\frac{\theta}{2}\cos\frac{3\theta}{2} + \frac{K_{II}}{\sqrt{2\pi r}}\cos\frac{\theta}{2}\left(1-\sin\frac{\theta}{2}\sin\frac{3\theta}{2}\right)$$

$$\tau_{xz} = -\frac{K_{III}}{\sqrt{2\pi r}}\sin\frac{\theta}{2}$$

$$\tau_{yz} = \frac{K_{III}}{\sqrt{2\pi r}}\cos\frac{\theta}{2}$$

$$u_x = \frac{K_I}{2G}\sqrt{\frac{r}{2\pi}}\cos\frac{\theta}{2}\left(\kappa-1+2\sin^2\frac{\theta}{2}\right) + \frac{K_{II}}{2G}\sqrt{\frac{r}{2\pi}}\sin\frac{\theta}{2}\left(\kappa+1+2\cos^2\frac{\theta}{2}\right)$$

$$u_y = \frac{K_I}{2G}\sqrt{\frac{r}{2\pi}}\sin\frac{\theta}{2}\left(\kappa+1-2\cos^2\frac{\theta}{2}\right)-\frac{K_{II}}{2G}\sqrt{\frac{r}{2\pi}}\cos\frac{\theta}{2}\left(\kappa-1-2\sin^2\frac{\theta}{2}\right)$$

$$u_z = \frac{K_{III}}{G}\sqrt{\frac{2r}{\pi}}\sin\frac{\theta}{2} \tag{2.2}$$

where K_I, K_{II} and K_{III} are the stress intensity factors that depend on the details of the geometry and loading, ν is Poisson's ratio, G is the shear modulus, and $\kappa = 3-4\nu$ ($\kappa = (3-\nu)/(1+\nu)$) for plane strain (plane stress). The three stress intensity factors represent the decomposition of the loading into three independent modes: tension (mode-I), in-plane shear (mode-II) and anti-plane shear (mode-III). The term universal is used because while the stress intensity factor for any given mode depends on the exact details of the geometry and loading, the r and θ dependence of the stress and displacement fields do not.

Stress intensity factor solutions can be obtained from numerous handbooks, including Tada et al. (1973). Consider for our discussion the symmetric loading ($K_{II} = K_{III} = 0$) of a crack of length $2a$ subjected to a uniform far-field tensile stress σ^∞ (Figure 2.3). For this case,

$$K_I = \sigma^\infty\sqrt{\pi a} \tag{2.3}$$

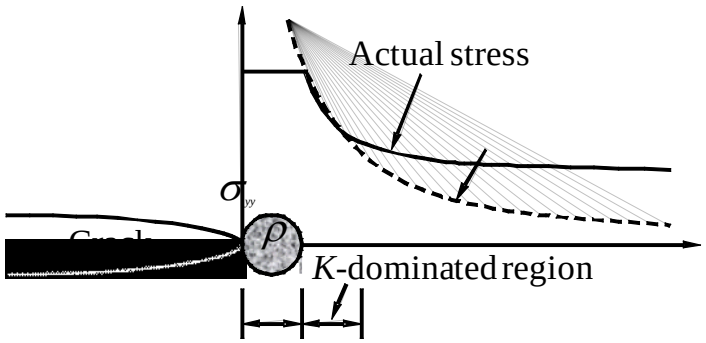

Figure 2.5. Schematic of stress field within and ahead of a process zone

The fracture toughness approach relies on the fact that as long as the irreversible deformation near the crack front resulting from the very high stresses (plastic yielding in metals, microcracking and aggregate interlock in concretes and other quasi-brittle materials, phase transformations in ceramics, etc.) is relatively small to other characteristic geometric dimensions (crack length for example), then the stress and displacement fields near a crack tip can be fully described through the single parameter K_I. Figure 2.5 is a schematic representation of the near tip region for such "small scale yielding" conditions (SSY). The crack tip is surrounded by a "process zone" wherein the high stresses have produced irreversible deformation. It has been shown through numerical simulations and experiments that if the extent of the process zone, ρ, is relatively small, then there exists a *K*-dominated region within an annulus extending from the edge of the process zone to a distance equal to a fraction of the crack length within which the

stresses and displacements are dominated by the singular terms associated with the elastic solution. In other words, all information from the "far field", which reflects the details of the structural geometry and applied loading, is transmitted to the crack-tip region through the stress intensity factor. It is then natural to assume that the crack will extend when the combination of loading and crack length produces a stress intensity factor, the one parameter characterizing the crack-tip region, equal to an experimentally measured critical value defined as the fracture toughness, K_{IC}, i.e.

$$K_I = K_{IC} \tag{2.4}$$

Irwin (1957) proved that the stress intensity factors that appear in Equation (2.2) are measures of the ERR, which represents the change in potential energy associated with the stresses ahead of the putative extension relaxing to zero while the surfaces of the extension open to their equilibrium configuration. In this work we limit ourselves to mode-I cracks, for which extension is self-similar. Then for an infinitesimal crack extension, Δa, Irwin showed that the ERR per unit thickness, G_I, is given by

$$G_I = \lim_{\Delta a \to 0} \frac{\int_0^{\Delta a} \frac{1}{2} \sigma_{yy}^b \delta^a dx}{\Delta a} \tag{2.5}$$

where σ_{yy}^b is the stress ahead of the crack before the extension given by Equation (2.2), and δ^a is the crack opening displacement after the extension. Substitution of the singular fields associated with the original crack and the extended crack leads to the Irwin relation:

$$G_I = \frac{K_I^2}{E'} \tag{2.6}$$

where $E' = E$ for plane stress, $E' = E/(1-\nu^2)$ for plane strain, and E is Young's modulus.

For the central crack subjected to a far-field tension,

$$G_I = \frac{\pi(\sigma^\infty)^2 a}{E'} \tag{2.7}$$

The fracture toughness criterion is thus equal to a critical ERR criterion:

$$G_I = G_{IC} \tag{2.8}$$

where G_{IC} is the critical ERR.

2.2.2 Nonlinear Fracture Mechanics

In concrete, asphalt and other quasi-brittle material structures with dimensions of practical relevance, the size of the process zone ahead of a crack does not satisfy SSY conditions, and therefore LEFM cannot be used to characterize crack propagation. However, the process zones in

these materials are confined to a narrow band ahead of a propagating crack, and they can be characterized by the CZM.

Barenblatt (1962) and Dugdale (1960) proposed similar analytical models that accounted for the zone near a crack tip within which irreversible deformations occur. The Dudgale model treats two thin process zones of length ρ ahead of the tips of a central crack in an otherwise linear elastic material subjected to far-field tension (Figure 2.6) as extensions of the main (traction-free) crack whose opening is resisted by a uniform distribution of tractions, σ_{ys}, that represent the rigid-perfectly plastic material ahead of the crack. Figure 2.6 shows the "cohesive law" for the Dudgale model, which represents the relation between the crack opening displacement and the traction that resists them. The cohesive law operates up to a critical value of the crack opening displacement, δ_c, where the stress drops to zero. Because the material is linear elastic, the far-field loading and the traction along the process zone both produce a stress intensity factor (the far-field produces a positive value and the closing tractions that resist crack opening produce a negative value). The physical model demands that the total stress intensity factor vanish (no infinite stresses are allowed)

$$K_{total} = K_I^{\infty} + K_I^{\sigma_{ys}} = 0 \tag{2.9}$$

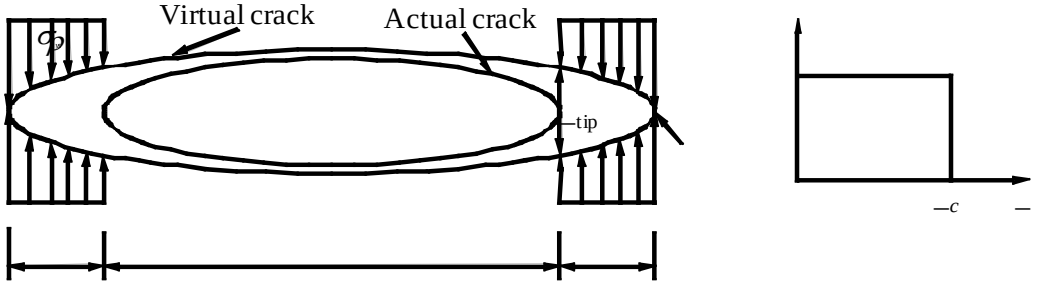

Figure 2.6. Dugdale model

Tada et al.'s handbook (1973) provides both stress intensity factor solutions:

$$K_I^{\infty} = \sigma^{\infty}\sqrt{\pi(a+\rho)} \tag{2.10}$$

$$K_I^{\sigma_{ys}} = -2\sigma_{ys}\sqrt{\frac{a+\rho}{\pi}}\cos^{-1}\left(\frac{a}{a+\rho}\right) \tag{2.11}$$

Equation (2.9) provides the normalized extent of the process zone in terms of the normalized applied stress:

$$\frac{\rho}{a} = \sec\frac{\pi\sigma^{\infty}}{2\sigma_{ys}} - 1 \tag{2.12}$$

$$\frac{\delta_{tip}}{a} = \frac{8\sigma_{ys}}{\pi E'} \log\left[\sec\left(\frac{\pi\sigma^{\infty}}{2\sigma_{ys}}\right)\right] \tag{2.13}$$

where δ_{tip} is the crack tip opening displacement (CTOD) of the actual crack as shown in Figure 2.6.

The crack is assumed to extend when the CTOD reaches the critical value (the material at the trailing edge of the process zone stretches to its capacity)

$$\delta_{tip} = \delta_c \tag{2.14}$$

Equation (2.14) provides the normalized critical stress

$$\frac{\sigma_c}{\sigma_{ys}} = \frac{2}{\pi}\cos^{-1}\left(e^{-\frac{\pi E'\delta_c}{8a\sigma_{ys}}}\right) \tag{2.15}$$

When $\rho / a \to 0$ or $\sigma^{\infty} / \sigma_{ys} \to 0$, SSY conditions are recovered:

$$\rho_{SSY} = \frac{\pi}{8}\left(\frac{K_I}{\sigma_{ys}}\right)^2 \tag{2.16}$$

$$\delta_{SSY} = \frac{K_I^2}{E'\sigma_{ys}} = \frac{G_I}{\sigma_{ys}} \tag{2.17}$$

$$\frac{\sigma_c}{\sigma_{ys}} = \frac{2\sqrt{2}}{\pi}\sqrt{\frac{\rho_{SSY}}{a}} \tag{2.18}$$

These equations show that for SSY setting the CTOD to a critical value is equivalent to setting the SIF and/or the ERR equal to their respective critical values.

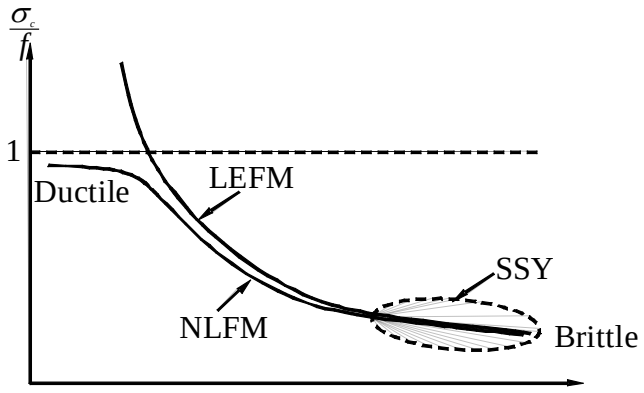

Figure 2.7. Transition between ductile and brittle response of a cracked structure

The transition from SSY conditions to "net-section yield" is illustrated in Figure 2.7, which shows the relationship between "structural size" or "brittleness number", defined as the ratio of crack length, a, to the SSY process zone size, ρ_{SSY} (Equation (2.16)), and normalized strength, σ_c / f_t (f_t is equal to σ_{ys} for the Dugdale model). When $a / \rho_{SSY} \to \infty$, the structure is brittle, and LEFM and NLFM predict the same strength. If $a / \rho_{SSY} \to 0$, the structure is ductile, and predicting ultimate capacity involves a simple limit load calculation. When a is comparable ρ_{SSY}, however, NLFM is required to predict capacity.

The Dugdale model was developed for steel plates subjected to plane stress conditions. Quasi-brittle materials such as concrete and asphalt are associated with strain-softening that corresponds to traction-separation relationships of the type shown in Figure 2.8. Hillerborg et al. (1976) extended the idea of the Dugdale model and proposed the CZM, also referred to as fictitious crack model. In the CZM, the crack path is a priori known, and the crack initiation and propagation are governed by the constitutive traction-separation relationship. The crack is assumed to initiate when the stress at the crack tip reaches the material tensile strength, f_t. When the crack opening displacement is smaller than the critical value of δ_c, that part of the crack still has the ability of stress transfer. The stress falls to zero when δ_c is reached. The critical ERR of the cohesive material is given by

$$G_F = \int_0^{\delta_c} \sigma(\delta) d\delta \tag{2.19}$$

which is the area under the traction-separation relationship and is equal to the required fracture energy per unit area to propagate the crack.

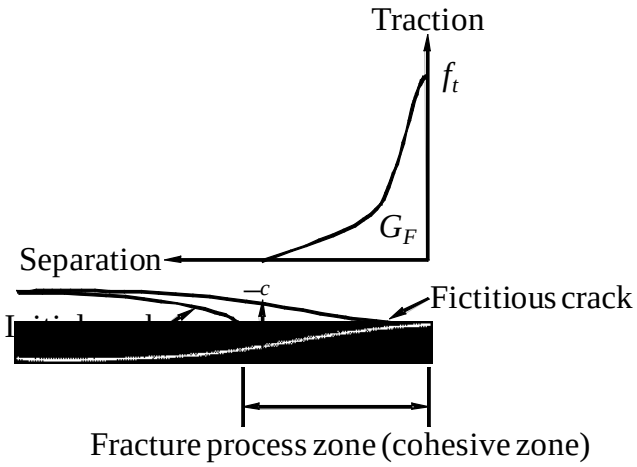

Figure 2.8. Cohesive zone model

2.2.3 CZMs for Concrete and Asphalt

CZMs assume that the cohesive law is a fundamental and unique material "property." The analysis of experiments using CZMs have convincingly demonstrated that ordinary concrete is

associated with strain-softening cohesive laws, and that the shapes of the curves that relate crack surface tractions to crack opening displacements for different concrete mixes have similar shapes (Petersson, 1981; Wittmann et al, 1988). Of the large number of shapes proposed in the literature, including linear (Hillerborg et al, 1976), bilinear (Petersson, 1981; Wittmann et al, 1988; Rokugo et al, 1989; Hilsdorf and Brameshuber, 1991), exponential (Gopalaratnam and Shah, 1985; Cornelissen et al, 1986; Planas and Elices, 1986), power-law (Reinhardt, 1984), and trilinear (Cho et al, 1984), the bilinear softening curve shown in Figure 2.9 is accepted as being the most accurate representations. Various dimensional coordinates of the kink point have been proposed, including ($\frac{2}{9}\delta_c$, $\frac{1}{3}f_t$) (Petersson, 1981), ($0.11\,\delta_c$-$0.15\,\delta_c$, $0.25\,f_t$) (Wittmann et al, 1988), and ($\frac{G_F - 22\delta_c\left(G_F / a_d\right)^{0.95}}{150(G_F / a_d)^{0.95}}$, $0.15\,f_t$) (Hilsdorf and Brameshuber, 1991). a_d is a coefficient depending on maximum aggregate size.

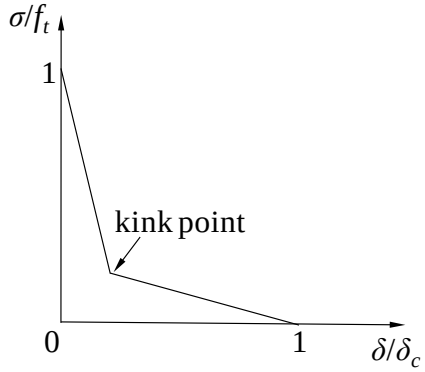

Figure 2.9. Bilinear softening cohesive law

Since the mid-1980s, a large number of experiments have been performed to characterize the bilinear softening curve through measurements of the tensile strength, f_t, and the fracture energy, G_F. The question of a proper fracture test standard was raised by Bazant (2002) and Bazant et al. (2002) in their proposal of a four parameter bilinear softening curve characterized by the initial fracture energy (the area under the first descending slope of the softening curve), the total fracture energy, the tensile strength, and the kink point coordinate. They pointed out that the initial fracture energy controls the load-carrying capacity of regular concrete structures.

An alternate method to construct the bilinear softening curve is to minimize the difference between numerical simulation results and experimental results by optimization. Park et al. (2008) briefly summarized the available literatures and, by conducting additional simulations and comparisons, concluded that the crack opening displacement at the kink point is equal to the structural critical CTOD.

Experimental and numerical investigations aimed at determination of the bilinear softening curve parameters continue (Roesler et al, 2007; Fathy et al, 2008; Elices et al, 2009; Morel et al, 2010). Bazant and Yu (2011) have pointed out that experiments using notched beams of similar sizes are not capable of determining the four parameters. Instead, beams of significantly different sizes are required in order to sample the whole curve; small specimens can be used to determine the

small crack opening displacement region, and large specimens with fully developed cohesive zones can be used to determine the large crack opening displacement region. Other methods used to determine the cohesive zone include Gain et al.'s (2011) hybrid experimental/numerical technique and Park et al.'s (2010) extension of CZMs for functionally graded fiber reinforced concrete.

2.2.4 Application of CZMs in Pavement Engineering

The application of fracture mechanics to pavement materials has been limited to monolithic components. Ioannides (1997, 2006) wrote a thorough literature review of research up to the mid-1990s, and suggested that fracture mechanics, combined with dimensional analysis, held the brightest promise for future concrete pavement design. A comprehensive review of fracture mechanics of AC is provided by Kim (2011), and experimental efforts to measure its fracture parameters include Jacobs et al. (1996), Marasteanu et al. (2002), Sangpetngam et al. (2003), Wagoner et al. (2005), Birgisson et al. (2008), Koh and Roque (2010), Li and Marasteanu (2010), and Dave et al. (2011). Testing configurations include single-edge notched beams, indirect tension, semicircular bending, disk-shaped compact tension, flattened indirect tension, and dog-bone direct tension. Song et al. (2006a, 2006b) and Kim et al. (2005, 2007) proposed CZMs for AC considering the viscoelasticity of the bulk material.

Ioannides and Sengupta (2003) have made important contribution to the application of the CZMs developed by the concrete fracture mechanics community to the design of concrete pavements. Their studies involve two-dimensional analyses of simply supported concrete beams, wherein progressive Mode-I crack propagation at the mid-span of the beam was simulated by a general-purpose finite element package and a FORTRAN code. The simulation results successfully reproduced experimental and numerical results obtained by other investigators. By plotting the ratio between the predicted ultimate bending strength and the material tensile strength, versus the structural brittleness number, with varying values of Young's modulus and specimen sizes while keeping the traction-separation relationship unchanged, a unique characteristic curve was produced. The uniqueness of the curve confirmed that the structural brittleness number generated size-independent results. This significant observation implied that probably a similar unique characteristic curve could be found for concrete pavements as well, as an improved mechanistic-based failure criterion.

The next step in their work was the extension of the CZM from two-dimensional simply supported beams to three-dimensional concrete pavement slabs using the finite element method program ABAQUS. Ioannides et al. (2006) modeled the slab resting on a Winkler foundation subjected to a single, square (or rectangular) edge load. Both notched and unnotched slabs were considered. The CZM was implemented by a series of spring-type elements. The effects of various loading parameters, notch size, size of the loaded area, slab thickness and slab size were examined.

Although the previous studies lead to improved understanding of the crack initiation and propagation in the concrete pavement slab, the modeling approach required significant efforts. Therefore, Gaedicke Hornung (2009) used the recent ABAQUS's built-in cohesive elements to implement the CZM for a systematic study on the fracture behavior of two-dimensional simply supported beams, two-dimensional beams on elastic foundations, three-dimensional simply

supported beams, and three-dimensional concrete pavement slabs, accompanying with respective experimental studies. Aure and Ioannides (2010) also investigated the ABAQUS's built-in cohesive elements by carrying out two-dimensional and three-dimensional simulations for crack propagation in concrete beams. The sensitivity of modeling procedures, such as mesh fineness and cohesive zone width, on the simulation results was scrutinized.

The CZM has also been applied to the fracture simulations of AC pavements. Examples of research efforts include Baek and Al-Qadi's (2008) study of reflection cracking mechanisms in AC overlays with interlayer systems, and Kim and Buttlar's (2009) investigation of low-temperature fracture behavior of AC airport pavements.

In summary, previous studies have focused on exploration of fracture mechanics modeling of pavements. They have not explored the insights of the simulation results, such as the previously discussed relationship between a composite pavement's ultimate load-carrying capacity and its material properties and geometric dimensions. These issues will be addressed in this research.

2.3 Summary

Current Minnesota procedures for UBCO design were reviewed. They are based on either empirical equations or highly simplified mechanistic models that do not account for strength-reducing geometric discontinuities and thus are questionable. Consequently, an argument for the use of a fracture mechanics design paradigm is put forth, because fracture mechanics is capable of capturing the effects of structural size on nominal strength, and of analyzing structures that contain crack-like flaws.

3 MODELING VERIFICATION

3.1 Introduction

Before using the CZM to simulate the failure of UBCOs, its finite element method implementation should be verified. In ABAQUS, the CZM can be implemented two different ways. The first involves cohesive elements that model the cohesive zone explicitly. However, this approach leads to lack of convergence and mesh dependency in strain-softening materials (SIMULIA, 2010), as illustrated in Appendix B. The second method, referred to as "Concrete Damaged Plasticity" model, uses conventional plane elements representing the cohesive zone. Our numerical experimentation showed that this latter method is sufficiently robust for the simulations considered in this research and was therefore adopted. To validate its implementation, several simulations were completed and the results were compared to available analytical or experimental data. Two fundamental examples are summarized as follows in Sections 3.2 and 3.3, respectively.

3.2 Infinite Plate with Circular Hole under Uniaxial Tension

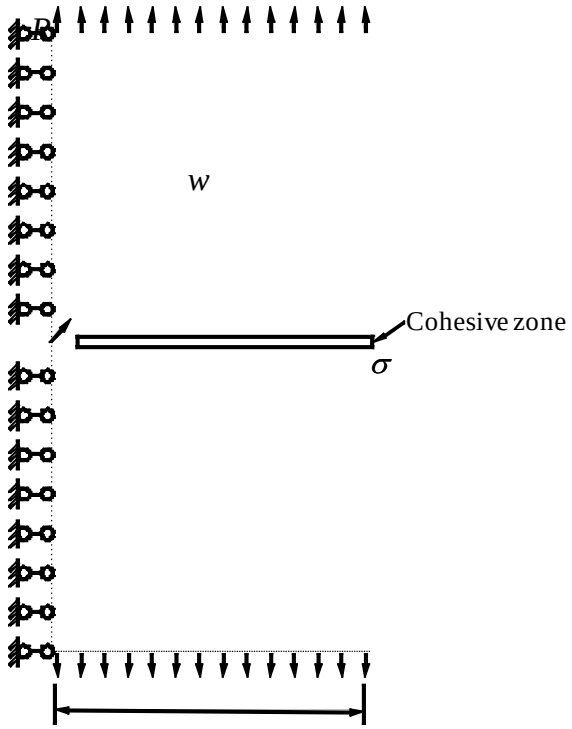

Figure 3.1. Mesh of a plate containing a circular hole and a cohesive zone

The configuration of this problem is similar to Figure 2.3. The infinite extension of the plate was approximated with a finite width ten times larger than the radius of the circular hole; $R / w = 0.1$. Because of symmetry, only one half of the plate was discretized as shown in Figure 3.1. Subsequent results represent plane stress conditions. First order quadrilateral plane stress elements, designated as CPS4 in ABAQUS, are used. A width of the cohesive zone equal to

$0.001\,w$ achieved an acceptable level of convergence of the load-displacement response. All subsequently presented results are associated with this value of width. A linear softening relationship for the traction-separation law was assumed, $\sigma = f_t\left(1-\frac{\delta}{\delta_c}\right)$ with f_t = 435 psi (3 MPa) and varying critical crack opening displacement. The elastic moduli are E = 4,350 ksi (30 GPa) and ν = 0.2.

The capacity of the plate was calculated by applying a displacement at its upper and lower edges. Figure 3.2 plots the normalized strength, σ_c / f_t, versus the structural size parameter, $\frac{R}{G_F E / f_t^2}$ (the denominator is again proportional to the size of the process zone ahead of the crack). As expected, when the structure is ductile the whole cross-section yields and the capacity approaches the tensile strength ($\sigma_c / f_t \to 1$); when the structure is brittle, on the other hand, the strength is reduced by the SCF ($\sigma_c / f_t \to 1/3$). Figure 3.3 shows illustrative tensile stress (in units of psi) distributions for both ductile ($\frac{R}{G_F E / f_t^2} = 0.2$) and brittle ($\frac{R}{G_F E / f_t^2} = 2.0$) cases when the strength is reached. When the structure is ductile, the size of the process zone is relatively large; when the structure is brittle, the size of the process zone is relatively small.

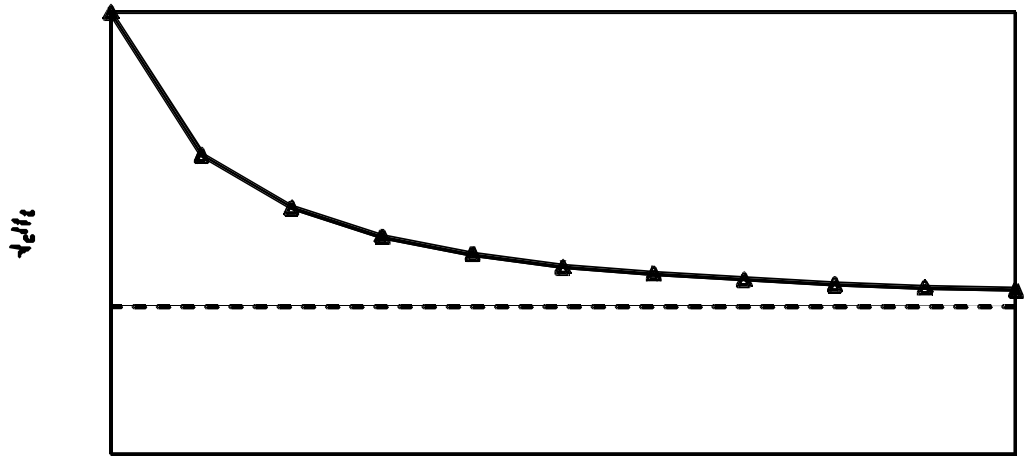

Figure 3.2. Normalized strength versus normalized structural size

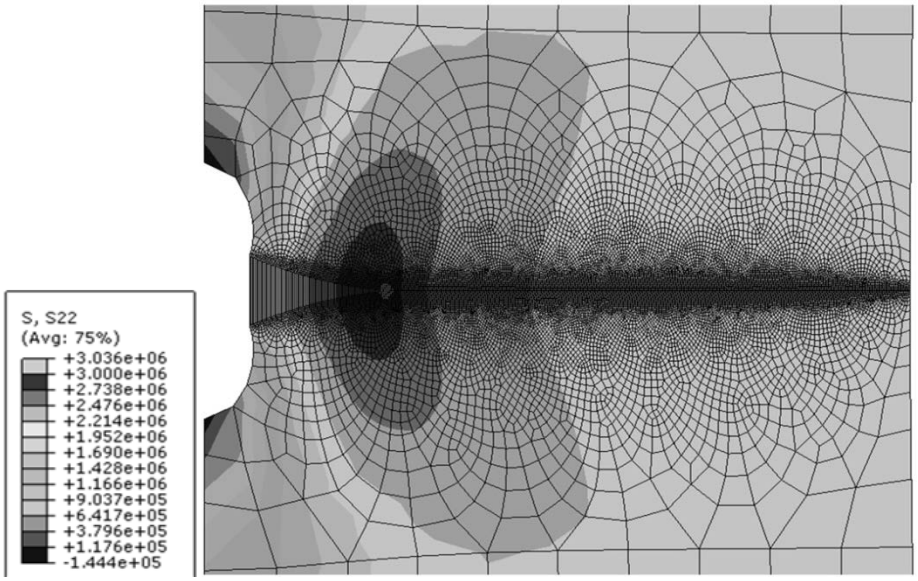

(a) Ductile: $\frac{R}{G_F E / f_t^2} = 0.2$

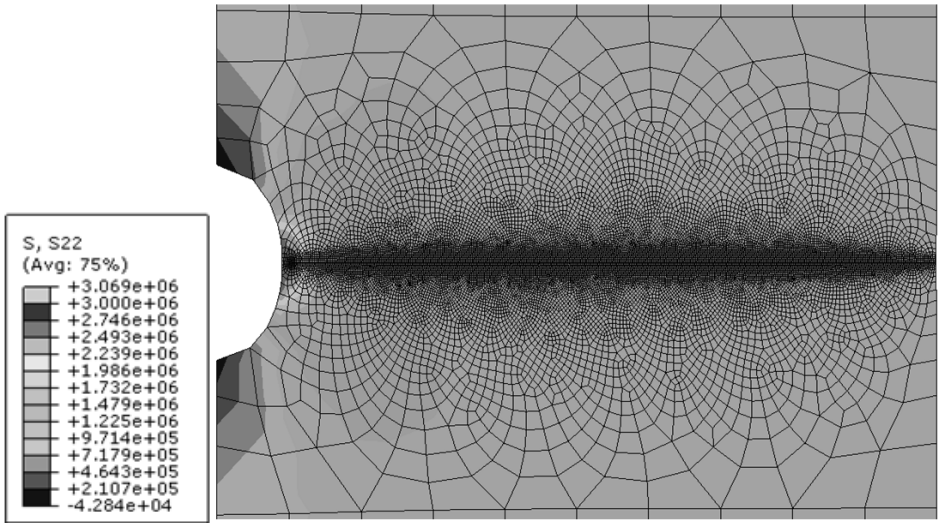

(b) Brittle: $\frac{R}{G_F E / f_t^2} = 2.0$

Figure 3.3. Tensile stress distributions along the cohesive zone

Figure 3.4 shows the development of the principal tensile stress along the cohesive zone for $\frac{R}{G_F E / f_t^2} = 0.2$ and four levels of normalized applied stresses: (a) before cracking when the principal tensile stresses along the whole cross-section are smaller than the tensile strength; (b) crack initiation when the principal tensile stress at the edge of the hole reaches the tensile strength; (c) crack extension when the crack tip propagates rightwards and the tensile stresses to the left of the crack tip are governed by the linear softening traction-separation law; (d) and

maximum load when the strength of the structure is reached. These plots verify that the stress distribution ahead of the crack satisfies the specified cohesive law.

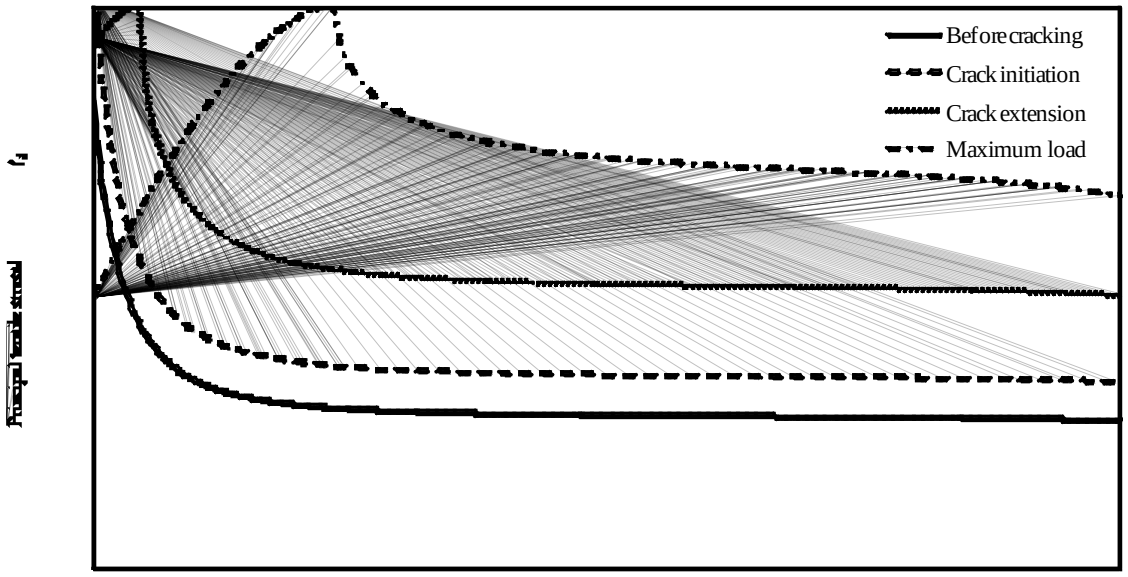

Figure 3.4. Development of principal tensile stresses along the cohesive zone

3.3 Notched Concrete Beam under Three-Point Bending

This problem was experimentally and numerically investigated by Gaedicke Hornung (2009). The beam is 43 inches (1,100 mm) long, 10 inches (250 mm) deep, and 3 inches (80 mm) wide. The span between the supports is 39 inches (1,000 mm). The notch to depth ratio is 1/3. Plane stress elements CPS4 in ABAQUS are employed and the discretized model is shown in Figure 3.5. The loading consists of a prescribed vertical displacement at mid-span. The material constants are E = 4,650 ksi (32.04 GPa), ν = 0.15, f_t = 600 psi (4.15 MPa) and G_F = 0.95 lb/inch (167 N/m).

Two cohesive laws with equal fracture energy were used as shown in Figure 3.6 (δ_c = 0.003 inches (0.08 mm) and 0.009 inches (0.24 mm), respectively). The stress at the kink point of the bilinear curve is equal to one quarter of the tensile strength. This exercise is used to demonstrate that for concrete the bilinear curve makes more accurate predictions of ultimate capacity than the linear curve. The load versus Crack Mouth Opening Displacement (CMOD) curves are shown in Figure 3.7. The linear relationship overestimates the load-carrying capacity, but the bilinear relationship shows good agreement with the experimental data. These findings agree with those of Gaedicke Hornung (2009).

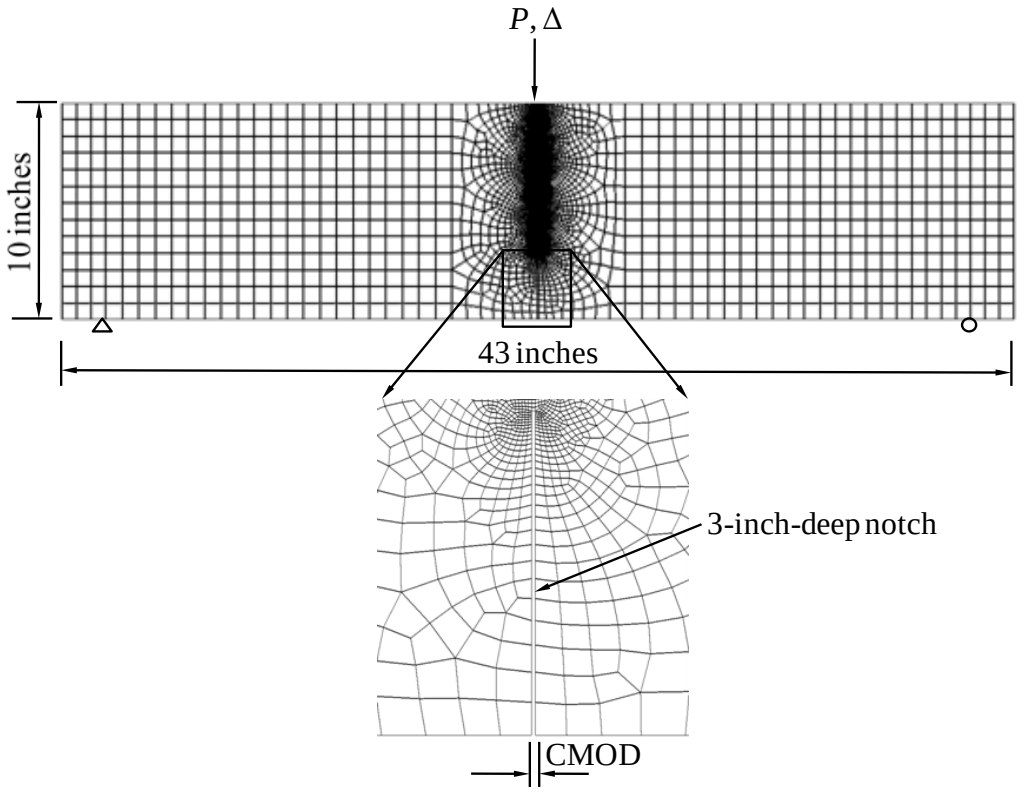

Figure 3.5. Finite element mesh of the concrete beam

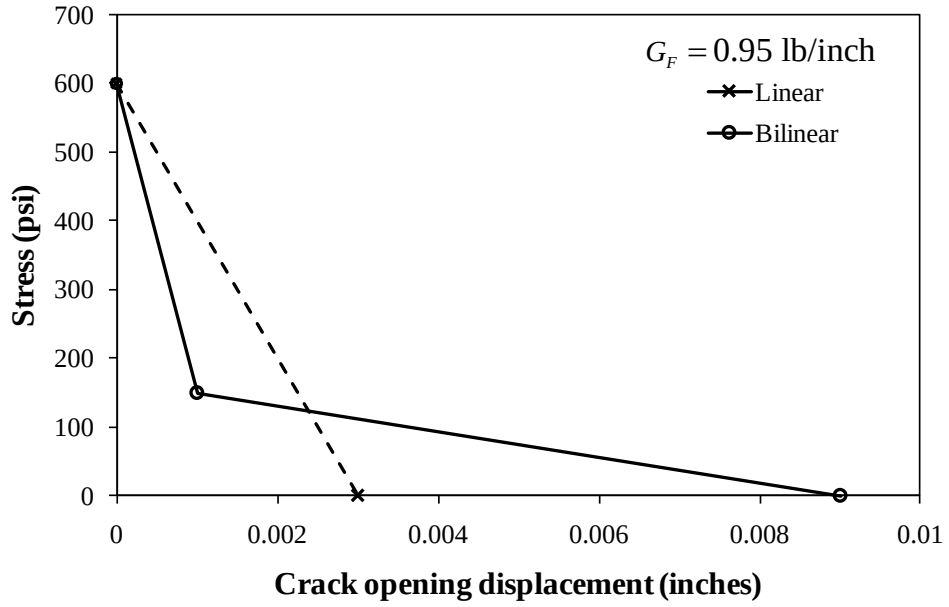

Figure 3.6. Approximate stress-crack opening displacement curves of concrete

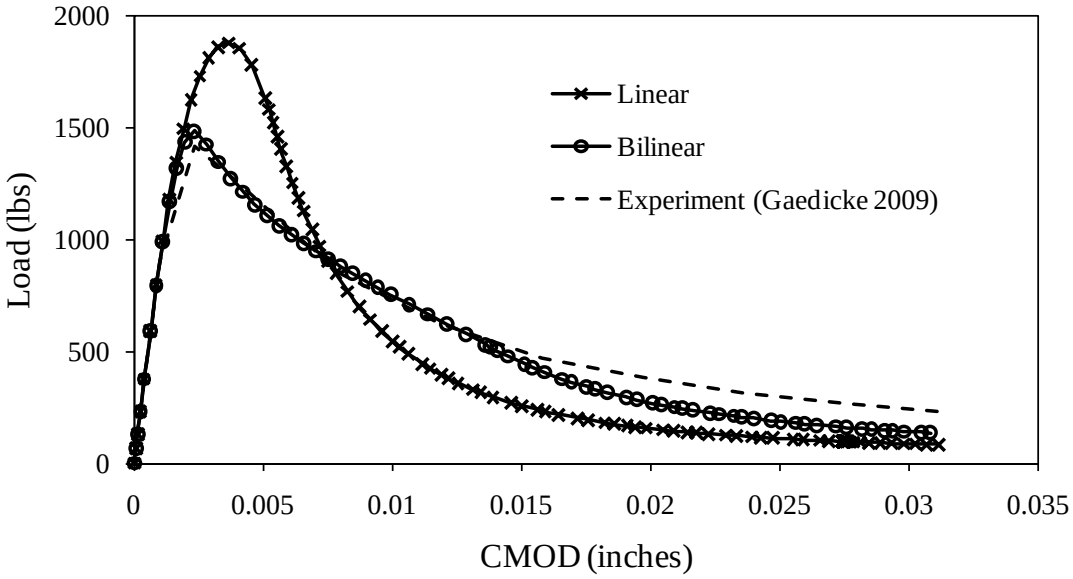

Figure 3.7. Load versus CMOD

3.4 Summary

A verification study of modeling has been carried out using ABAQUS. The simulation results have validated its capability of using the CZM to simulate crack initiation and extension in quasi-brittle materials. Similar modeling process will be employed to create single-layer pavement models and UBCO models in the next chapters.

4 SINGLE-LAYER PCC PAVEMENT

4.1 Introduction

As discussed in Chapter 1, pavement engineers have developed relatively robust design procedures for single-layer PCC pavements. Therefore, a fracture mechanics-based structural equivalency approach has been proposed to design UBCOs. The first step of the approach is to analyze the single-layer (reference) pavement using the CZM. Section 4.2 presents the mechanistic model calculated using the ABAQUS implementation of the CZM described in Chapter 3. An illustrative example is presented to demonstrate the model's capability. Section 4.3 explores a universal relationship derived from the large number of simulations between the load-carrying capacity of the single-layer pavement and the brittleness number.

4.2 Finite Element Model

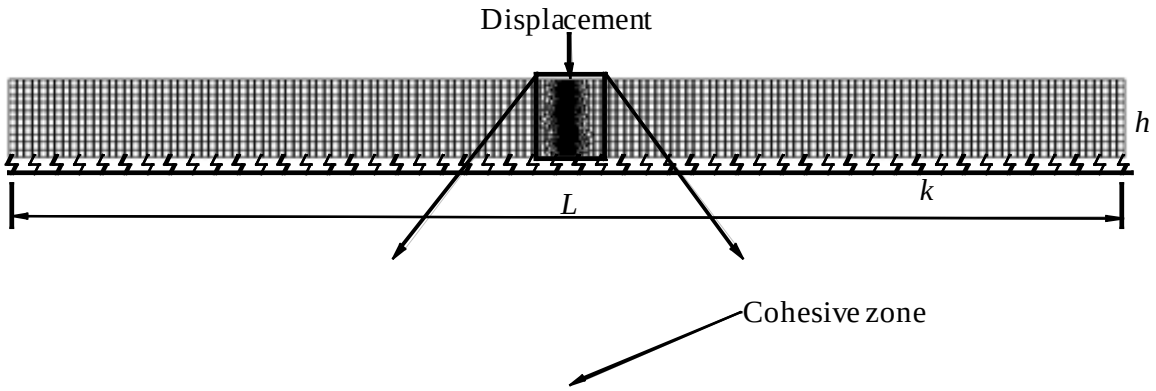

Figure 4.1. Cohesive zone model of a single-layer PCC pavement

The plane strain model of a single-layer PCC pavement of length, L, depth, h, and thickness, b, resting on a Winkler foundation (Westergaard, 1947) with stiffness, k, is shown in Figure 4.1. The pavement is assumed to be fully bonded with the foundation, and thus potential separation between the pavement and the foundation is not simulated. In addition, pavement joint load transfer is not considered in this research; the ends of the pavement are free to rotate. Failure is assumed to result from the initiation and subsequent propagation of a cohesive edge crack at the point of maximum tensile stress.

The CZM assumes that the crack opening displacement at each point along the crack surfaces, δ, is resisted by a conjugate traction, σ. A bilinear softening traction-separation relationship similar to the one proposed by Wittmann et al. (1988) shown in Figure 4.2 is adopted in this

research. The coordinates of the kink point are ($0.125\,\delta_c$, $0.25\,f_t$). According to Bazant (2002), the initial fracture energy controls the maximum load of ordinary concrete structures. Since the change in abscissa of the kink point is equal to only 1/8 of the change in abscissa of δ_c, a constant δ_c = 0.008 inches (0.2 mm) is used in all subsequent simulations (Wittmann et al, 1988). This implies that the total fracture energy G_F is solely a function of f_t. The cohesive zone is implemented using the "concrete damaged plasticity" material properties in ABAQUS, for which the σ-δ relationship is input in tabular form. The material model involves a scalar tension damage parameter that is also input as a tabular function of δ. The damage parameter is set equal to zero when the crack opening displacement is zero and 0.9 when δ reaches δ_c. The aspect ratio of the elements within the cohesive zone is made equal to 1.0 in order to mitigate mesh sensitivity.

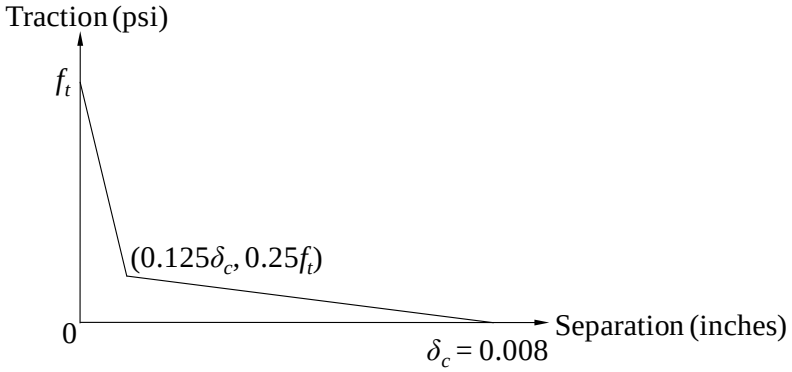

Figure 4.2. Bilinear traction-separation relationship of concrete

The fracture energy introduces a characteristic length, which is proportional to the length of the process zone in the vicinity of the crack front, defined by

$$l_{ch} = \frac{EG_F}{f_t^2} \tag{4.1}$$

where E is the Young's modulus. The pavement is expected to behave in a brittle (ductile) manner if h / l_{ch} is large (small).

A 0.1-inch-thick (2.54-mm-thick) cohesive zone is placed at the mid-span of the slab through the whole depth to simulate crack initiation and propagation under displacement control. First order quadrilateral plane strain elements, designated as CPE4 in ABAQUS, are assigned to all elements. The elements outside the cohesive zone are linear elastic. The algorithm used to solve the finite element equations relies on the Riks method because it is capable of capturing the snap-back instabilities associated with relatively high values of h / l_{ch}.

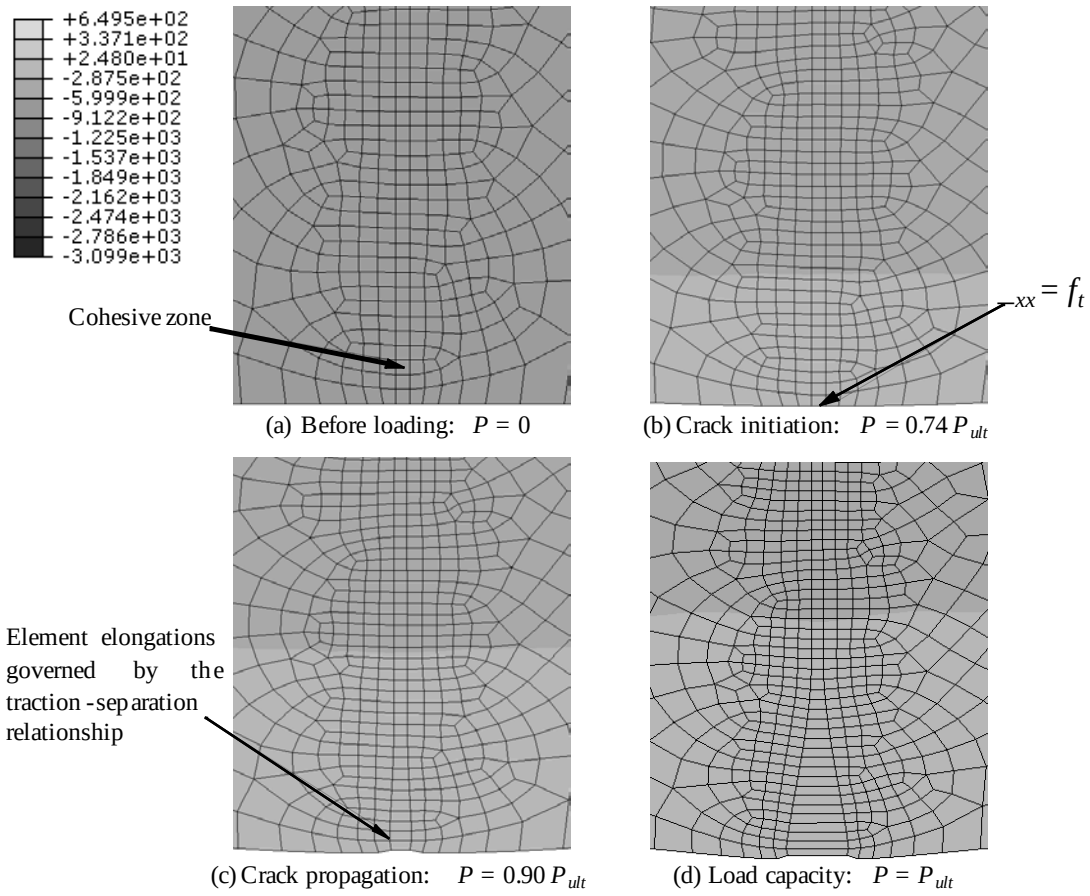

Figure 4.3. Deformation and tensile stress distribution along the cohesive zone

Figure 4.3 illustrates the CZM's ability to capture the localized deformation in the region that initiates the crack for the illustrative parameters, L = 12 feet (3.66 m), h = 10 inches (0.25 m), E = 4,000 ksi (27.58 GPa), f_t = 450 psi (3.10 MPa), G_F = 0.675 lb/inch (118.21 N/m), k = 100 pci (27.14 MPa/m), and Poisson's ratio ν = 0.20. These plots show the 2000X-amplified mesh deformation, upon which the horizontal stress component contours (in units of psi), σ_{xx}, are superimposed. Four instants of the loading history are shown. (a) corresponds to the unloaded reference state; (b) shows the point at which the tensile stress at the trail end of the cohesive zone reaches the tensile strength, f_t. At this point, where the reaction force at the loaded nodes is approximately 74% of the maximum load, P_{ult}, the cohesive zone starts to unzip; (c) indicates that at $0.9\,P_{ult}$ the cohesive elements are clearly stretched; (d) the load capacity P_{ult} is reached.

4.3 Normalized Load Capacity

The structural system of the single-layer pavement involves the independent physical parameters P_{ult}, L, b, h, E, f_t, G_F, and k. Since G_F is a function of only f_t, seven physical parameters are independent. They are expressible in terms of three independent fundamental physical quantities: mass, length, and time. Buckingham's π theorem (Buckingham, 1914) states that if a system involves n physical parameters that are expressible in terms of m independent

fundamental physical quantities, then $n-m$ dimensionless parameters are required to fully describe the system. Therefore, four dimensionless parameters are required for the single-layer pavement. The following normalization choices reduce subsequent parameter studies. All dimensions are normalized with respect to L, l_{ch} and the radius of relative stiffness

$$l = \sqrt[4]{\frac{D}{k}} \tag{4.2}$$

where

$$D = \frac{Eh^3}{12(1-\nu^2)} \tag{4.3}$$

In the absence of the Winkler foundation, three dimensionless parameters are required: h/L, h/l_{ch}, and normalized load capacity. The normalized load capacity is defined as the ratio of modulus of rupture (MOR) to f_t and is written in terms of the bending moment at the loading point, M, as $\frac{6M}{bh^2 f_t} = \frac{3P_{ult}L}{2bh^2 f_t}$. Since the influence of h/L is insignificant for relatively slender beams (Ioannides and Sengupta, 2003), the normalized load capacity is plotted as a function of h/l_{ch} in Figure 4.5. This plot illustrates the previously discussed transition from ductile to brittle structural response of quasi-brittle materials. The curve can be approximated by the equation

$$\frac{3P_{ult}L}{2bh^2 f_t} = 3.76\left(\frac{h}{l_{ch}}\right)^4 - 9.33\left(\frac{h}{l_{ch}}\right)^3 + 8.74\left(\frac{h}{l_{ch}}\right)^2 - 3.84\left(\frac{h}{l_{ch}}\right) + 2.04 \tag{4.4}$$

In the presence of the Winkler foundation, the bending moment at the loading point (Boresi and Schmidt, 2003) is written as

$$M = \frac{\sqrt[4]{4\left(1-\nu^2\right)}}{4} P_{ult} l \Phi \tag{4.5}$$

where

$$\Phi = \frac{\cosh\left[\frac{1}{\sqrt[4]{4\left(1-\nu^2\right)}}\frac{L}{l}\right] - \cos\left[\frac{1}{\sqrt[4]{4\left(1-\nu^2\right)}}\frac{L}{l}\right]}{\sinh\left[\frac{1}{\sqrt[4]{4\left(1-\nu^2\right)}}\frac{L}{l}\right] + \sin\left[\frac{1}{\sqrt[4]{4\left(1-\nu^2\right)}}\frac{L}{l}\right]} \tag{4.6}$$

The derivation of Equations (4.5) and (4.6) is included in Appendix C. Figure 4.4 plots Φ versus L/l with $\nu = 0.2$. The curve suggests that when L/l is relatively small, it has significant influences on the bending moment. However, if L/l is large enough, $\Phi \to 1$ and the bending moment approaches the solution of an infinite beam resting on the foundation.

Consequently, the natural choice for normalized load capacity is $\frac{6M}{bh^2 f_t} = \frac{3\sqrt[4]{4\left(1-\nu^2\right)}P_{ult} l\Phi}{2bh^2 f_t}$, which is plotted in Figure 4.5 for practical values of h/l = 0.21, 0.27, and 0.32, respectively. In addition, Figure 4.5 shows the sensitivity of the normalized load capacity on h/L for constant values of h/l. For convenience, the ABAQUS simulations can be run in a batch mode in conjunction with a general purpose software toolkit, named as Design Analysis Kit for Optimization and Terascale Applications (DAKOTA) which is developed by the Sandia National Laboratories (Adams et al, 2009). Details about its implementation are included in Appendix D. The results in Figure 4.5 suggest that for the practical range of the relevant parameters, the various curves of this choice of normalized capacity can be collapsed into the following equation

$$\frac{3\sqrt[4]{4\left(1-\nu^2\right)}P_{ult} l\Phi}{2bh^2 f_t} = 5.41\left(\frac{h}{l_{ch}}\right)^4 - 13.44\left(\frac{h}{l_{ch}}\right)^3 + 12.56\left(\frac{h}{l_{ch}}\right)^2 - 5.40\left(\frac{h}{l_{ch}}\right) + 2.35 \qquad (4.7)$$

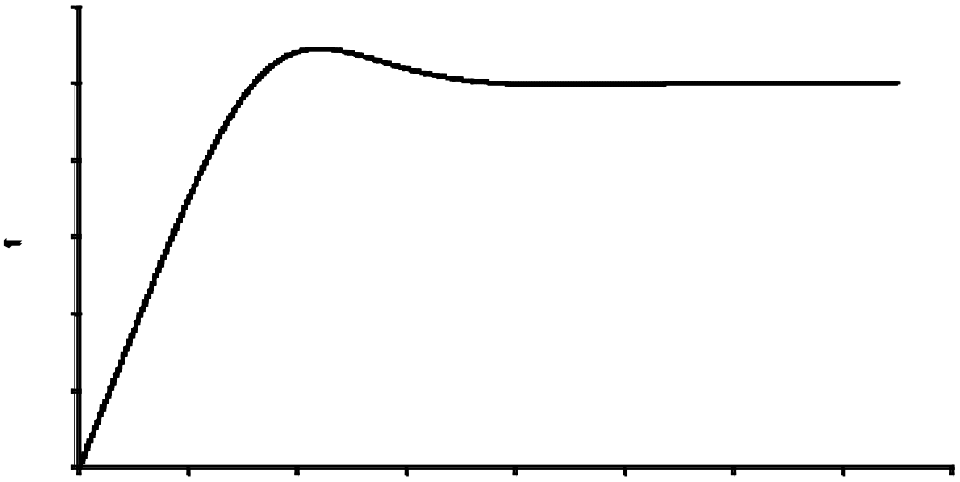

Figure 4.4. Φ **versus** L/l

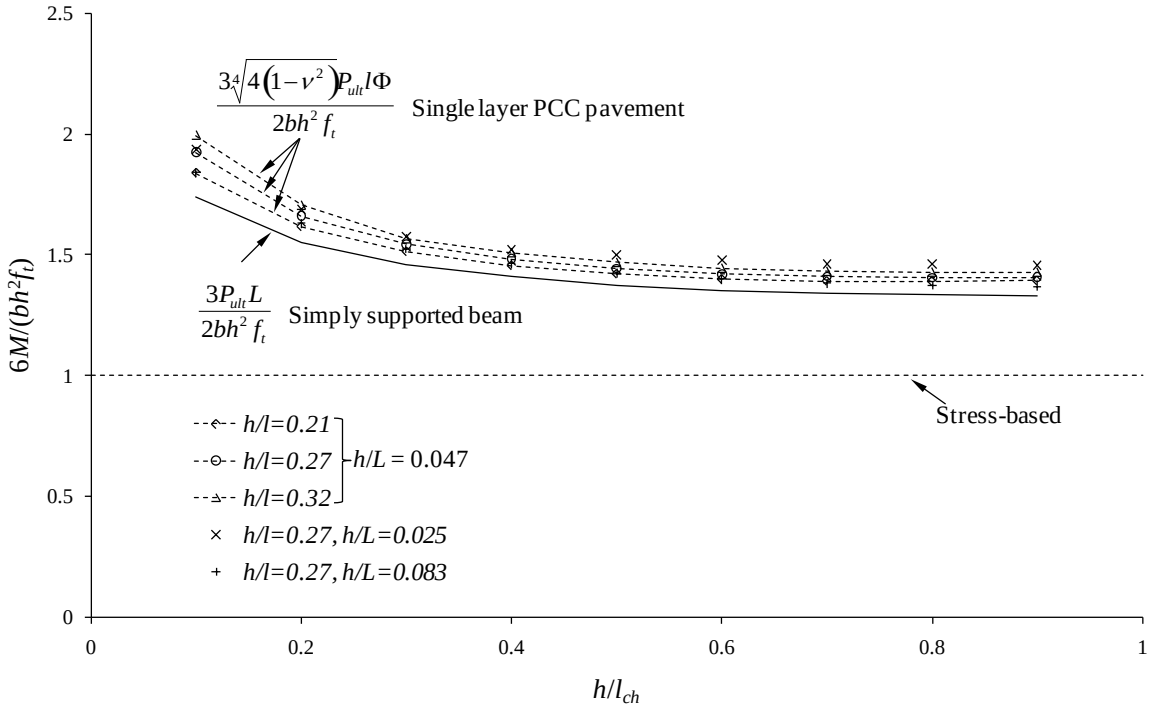

Figure 4.5. Normalized load capacity versus h / l_{ch}

4.4 Summary

A finite element-based CZM for single-layer PCC pavements have been created using ABAQUS and a bilinear traction-separation relationship that best accounts for the post-peak behavior of concrete. The illustrative example demonstrates the model's ability to capture crack initiation and propagation. The normalized load-carrying capacity can be adequately expressed in terms of the single structural size parameter h / l_{ch}.

5 UNBONDED CONCRETE OVERLAY PAVEMENT

5.1 Introduction

This chapter applies the CZM to UBCOs to analyze the characteristics of their fracture behavior. Section 5.2 defines the finite element models. Because the UBCO system is a composite system, the number of physical parameters that govern the load-carrying capacity is much larger than the number associated with the single-layer pavement. Determining the relationship between the load capacity and the material properties and geometry is not as apparent, and thus a dimensional analysis procedure is employed to simplify the process. A relationship between the load-carrying capacity and the geometric and material parameters is derived. Combining the load-carrying capacity equations of the single-layer pavement and the UBCO in Section 5.3 leads to a design procedure for UBCOs based on structural equivalency.

5.2 Finite Element Model

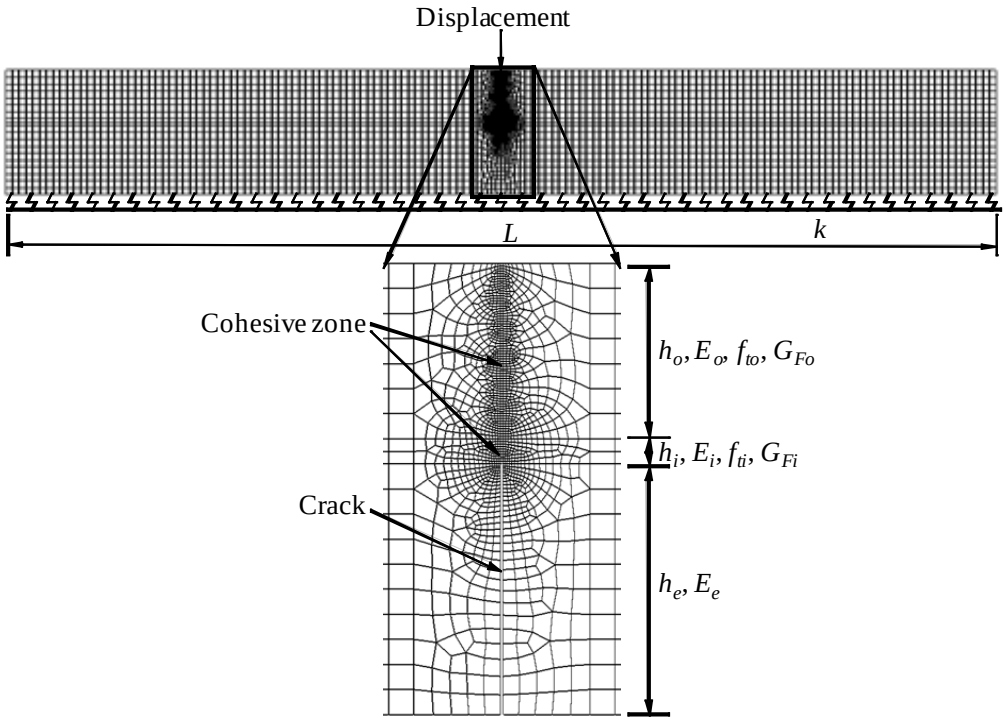

Figure 5.1. Cohesive zone model of an UBCO system

The configuration and finite element model of the UBCO is shown in Figure 5.1. The PCC overlay, AC interlayer, and existing PCC pavement have thicknesses h_o, h_i, and h_e, and material properties E_o, E_i, E_e, f_{to}, f_{ti}, G_{Fo}, and G_{Fi}, respectively. The ends of each layer are free to rotate and are thus representative of pavements with zero joint load transfer efficiency. Between each layer, the interfaces are fully bonded to represent the cohesion of the AC interlayer. The separation between the foundation and the existing pavement is not considered. The cohesive laws of the overlay and the interlayer have equal shapes as the one used for the single-layer

pavement. However, a larger critical crack opening displacement δ_c = 0.02 inches (0.5 mm) is used for AC.

Reflection cracking within the overlay is assumed to initiate from one preexisting 0.1-inch-thick (2.54-mm-thick) crack at the mid-span of the existing PCC pavement. Note that in the simulations cracking could initiate and propagate through the interlayer before cracking initiates in the overlay, or it could initiate in the overlay before cracking in the interlayer propagates through the interlayer, depending on the relative values of fracture toughness. For example, Figure 5.2 shows the 30X-amplified mesh deformations and the stress component σ_{xx} contours (in units of psi) when L = 12 feet (3.66 m), k = 100 pci (27.14 MPa/m), h_o = 6 inches (15.24 cm), h_i = 1 inch (2.54 cm), h_e = 10 inches (25.40 cm), E_o = 4,000 ksi (27.58 GPa), E_i = 500 ksi (3.45 GPa), E_e = 6,000 ksi (41.37 GPa), f_{to} = 450 psi (3.10 MPa), f_{ti} = 400 psi (2.76 MPa), G_{Fo} = 0.675 lb/inch (118.21 N/m), and G_{Fi} = 1.5 lb/inch (262.69 N/m). A crack initiates in the interlayer. However, before this crack propagates through the interlayer, another crack initiates in the overlay since the interlayer has much higher fracture toughness than the overlay.

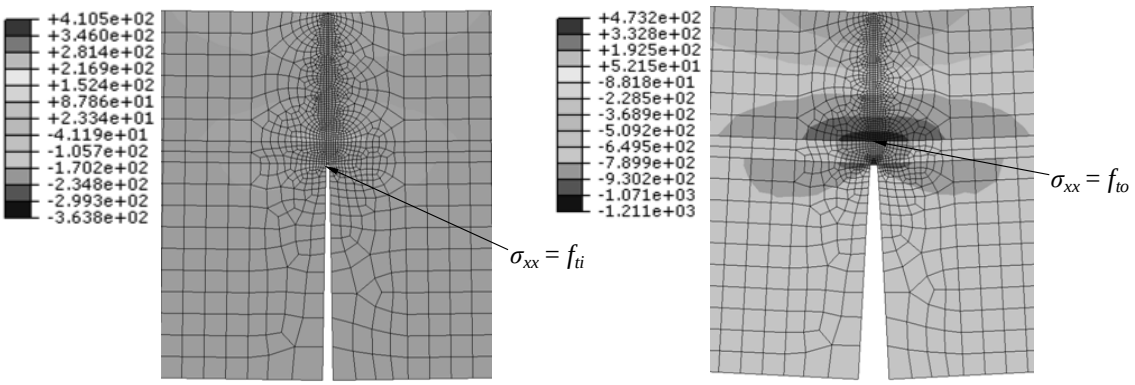

(a) Crack initiation in interlayer (b) Crack initiation in overlay

Figure 5.2. Illustrative crack initiation and propagation

The UBCO composite involves many more physical parameters than the single-layer PCC pavement: P_{ult}, b, L, k, h_o, h_i, h_e, E_o, E_i, E_e, f_{to}, f_{ti}, G_{Fo}, and G_{Fi}. Since G_{Fo} and G_{Fi} are functions of f_{to} and f_{ti}, respectively, twelve physical parameters are independent. According to the Buckingham's π theorem (Buckingham, 1914), nine dimensionless parameters are necessary to fully describe the system. The normalized load capacity is $\frac{P_{ult}}{bh_o f_{to}}$, and it is a function of the eight dimensionless quantities: h_o / l_{cho}, h_i / l_{chi}, E_o / E_i, E_o / E_e, h_o / h_i, h_o / h_e, h_o / L, and kh_o / E_o, where l_{cho} and l_{chi} are the characteristic lengths of the PCC overlay and the AC interlayer, respectively.

A relationship between the capacity and the independent variables was derived for h_o = 4, 5, 6, 7, and 8 inches (10.16, 12.70, 15.24, 17.78, and 20.32 cm), respectively, by consecutively sweeping

through a practical range of one independent variable while keeping the rest constant using DAKOTA. The range of each parameter is: L = 12-20 feet (3.66-6.10 m), k = 100-300 pci (27.14-81.43 MPa/m), h_i = 0.5-2 inches (1.27-5.08 cm), h_e = 6-12 inches (15.24-30.48 cm), E_o = 4,000 ksi (27.58 GPa), E_i = 500-1,500 ksi (3.45-10.34 GPa), E_e = 5,000-9,000 ksi (34.47-62.05 GPa), f_{to} = 400-600 psi (2.76-4.14 MPa), f_{ti} = 400-600 psi (2.76-4.14 MPa), G_{Fo} = 0.6-0.9 lb/inch (105.08-157.61 N/m), and G_{Fi} = 1.5-2.25 lb/inch (262.69-394.04 N/m). The results are presented in tabular form in Appendix E. The results imply that the relationship between the normalized load capacity and the independent variables can be approximated as a combination of power law and polynomial equation, wherein the exponents and the polynomial coefficients were calculated using a least squares analysis of the capacities. The derived relationships are

h_o = 4 inches (10.16 cm):

$$\frac{P_{ult}}{bh_o f_{to}} = 10^4 \left(\frac{h_o}{l_{cho}}\right)^{-0.60} \left(\frac{h_i}{l_{chi}}\right)^{0.49} \left(\frac{E_o}{E_i}\right)^{-0.30} \left(\frac{E_o}{E_e}\right)^{0.05} \left(\frac{h_o}{h_i}\right)^{0.13} \left(\frac{h_o}{h_e}\right)^{0.01} \left(\frac{kh_o}{E_o}\right)^{0.54} \left[8.4667\left(\frac{h_o}{L}\right)^2 - 0.4860\left(\frac{h_o}{L}\right) + 0.0101\right] \tag{5.1a}$$

h_o = 5 inches (12.70 cm):

$$\frac{P_{ult}}{bh_o f_{to}} = 10^4 \left(\frac{h_o}{l_{cho}}\right)^{-0.62} \left(\frac{h_i}{l_{chi}}\right)^{0.50} \left(\frac{E_o}{E_i}\right)^{-0.32} \left(\frac{E_o}{E_e}\right)^{0.06} \left(\frac{h_o}{h_i}\right)^{0.13} \left(\frac{h_o}{h_e}\right)^{0.04} \left(\frac{kh_o}{E_o}\right)^{0.48} \left[2.8756\left(\frac{h_o}{L}\right)^2 - 0.1911\left(\frac{h_o}{L}\right) + 0.0050\right] \tag{5.1b}$$

h_o = 6 inches (15.24 cm):

$$\frac{P_{ult}}{bh_o f_{to}} = 10^4 \left(\frac{h_o}{l_{cho}}\right)^{-0.60} \left(\frac{h_i}{l_{chi}}\right)^{0.51} \left(\frac{E_o}{E_i}\right)^{-0.33} \left(\frac{E_o}{E_e}\right)^{0.07} \left(\frac{h_o}{h_i}\right)^{0.12} \left(\frac{h_o}{h_e}\right)^{0.05} \left(\frac{kh_o}{E_o}\right)^{0.41} \left[1.0627\left(\frac{h_o}{L}\right)^2 - 0.0785\left(\frac{h_o}{L}\right) + 0.0025\right] \tag{5.1c}$$

h_o = 7 inches (17.78 cm):

$$\frac{P_{ult}}{bh_o f_{to}} = 10^3 \left(\frac{h_o}{l_{cho}}\right)^{-0.59} \left(\frac{h_i}{l_{chi}}\right)^{0.48} \left(\frac{E_o}{E_i}\right)^{-0.33} \left(\frac{E_o}{E_e}\right)^{0.07} \left(\frac{h_o}{h_i}\right)^{0.11} \left(\frac{h_o}{h_e}\right)^{0.07} \left(\frac{kh_o}{E_o}\right)^{0.34} \left[3.8264\left(\frac{h_o}{L}\right)^2 - 0.3043\left(\frac{h_o}{L}\right) + 0.0118\right] \tag{5.1d}$$

h_o = 8 inches (20.32 cm):

$$\frac{P_{ult}}{bh_o f_{to}} = 10^3 \left(\frac{h_o}{l_{cho}}\right)^{-0.53} \left(\frac{h_i}{l_{chi}}\right)^{0.51} \left(\frac{E_o}{E_i}\right)^{-0.32} \left(\frac{E_o}{E_e}\right)^{0.07} \left(\frac{h_o}{h_i}\right)^{0.11} \left(\frac{h_o}{h_e}\right)^{0.07} \left(\frac{kh_o}{E_o}\right)^{0.30} \left[2.1634\left(\frac{h_o}{L}\right)^2 - 0.1798\left(\frac{h_o}{L}\right) + 0.0082\right] \quad (5.1e)$$

The equations listed above are plotted in Figure 5.3 together with the results of the simulations and with results of simulations performed for random choices of the parameters within the stated ranges (which are also included in Appendix E). The agreement between the regressions and the simulations is deemed acceptable for all intents and purposes.

The ultimate capacity equations can be further simplified for the practical range considered in this research (E_e = 5,000-9,000 ksi (34.47-62.05 GPa), h_e = 6-12 inches (15.24-30.48 cm)) by noting that the exponents associated with E_o / E_e and h_o / h_e are nearly zero. It is noted that the near independence of the ultimate load capacity on the stiffness and thickness of the existing pavement is in contrast with currently available design formulas, which state that thicker existing pavements require thinner UBCOs.

Equation (5.1) also sheds insights on how to improve the ultimate capacity. It suggests that the load capacity is most sensitive to h_o / l_{cho} and h_i / l_{chi}. Therefore, the most effective ways of increasing capacity are to increase the toughness (actually the tensile strength since the critical crack opening displacement is assumed to be a constant value) of the overlay and/or the interlayer. Larger foundation stiffness k, increasing the thickness of the interlayer h_i, and decreasing the stiffness of the interlayer E_i also result in increased ultimate capacity.

The influence of the overlay length L is not monotonic since the separation between the UBCO pavement and the foundation is not considered. When h_o / L is relatively large, there is no separation and the foundation is in full compression. The load capacity decreases as L increases. However, when L increases beyond a certain length, the foundation at the ends of the pavement carries relatively small tension forces that result in an increase in the ultimate capacity.

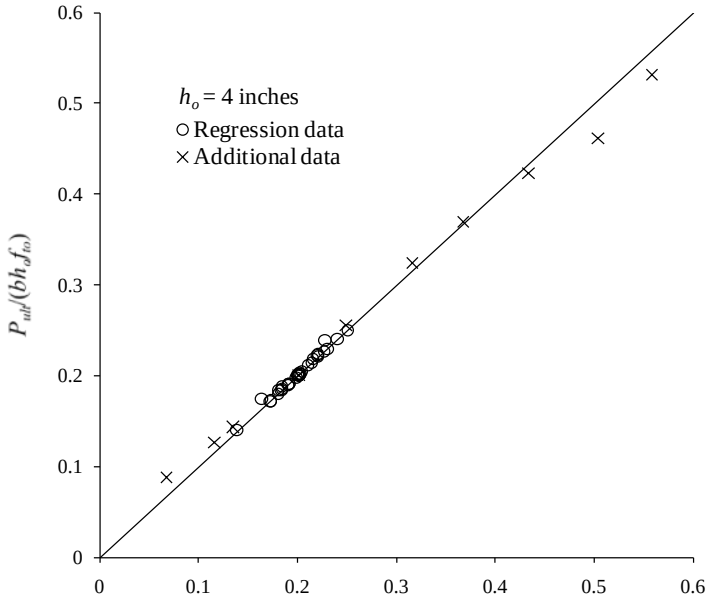

(a) h_o = 4 inches (10.16 cm)

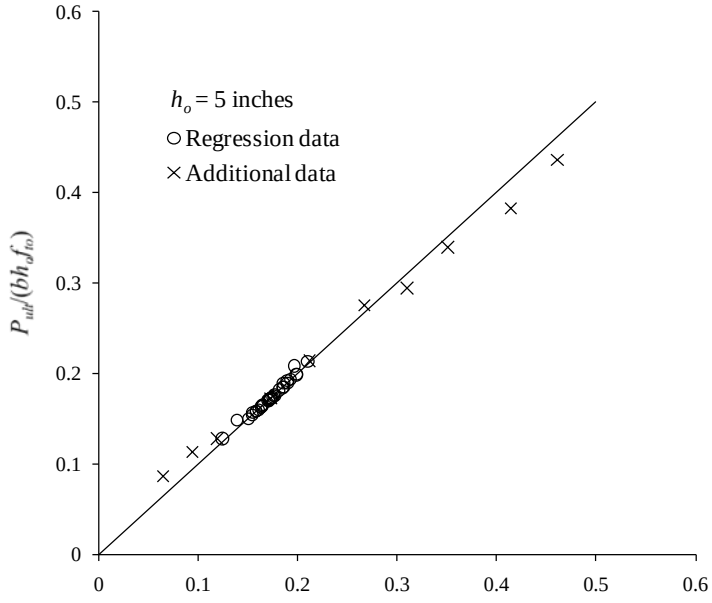

(b) h_o = 5 inches (12.70 cm)

Figure 5.3. Derived relationship between the capacity and the variables

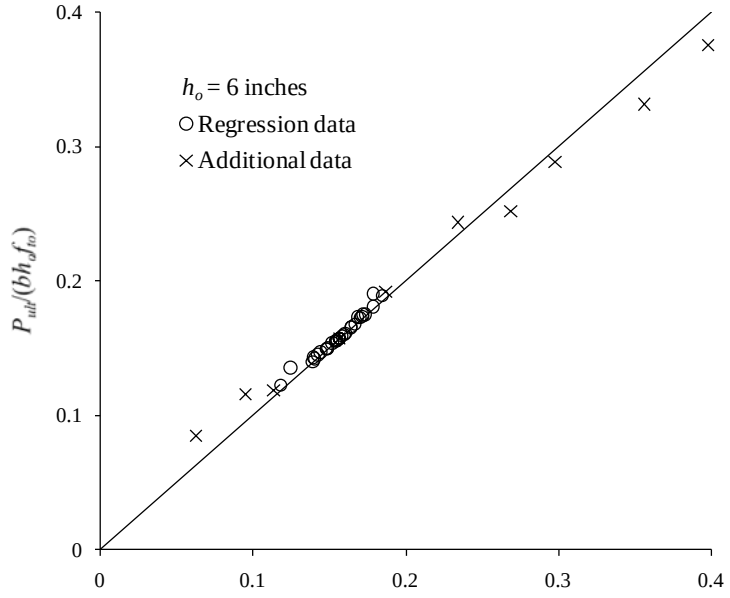

(c) h_o = 6 inches (15.24 cm)

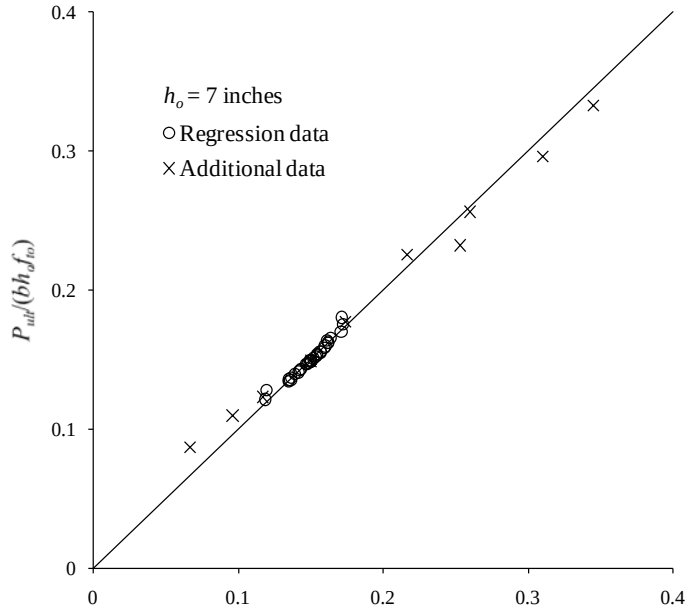

(d) h_o = 7 inches (17.78 cm)

Figure 5.3. (continued) Derived relationship between the capacity and the variables

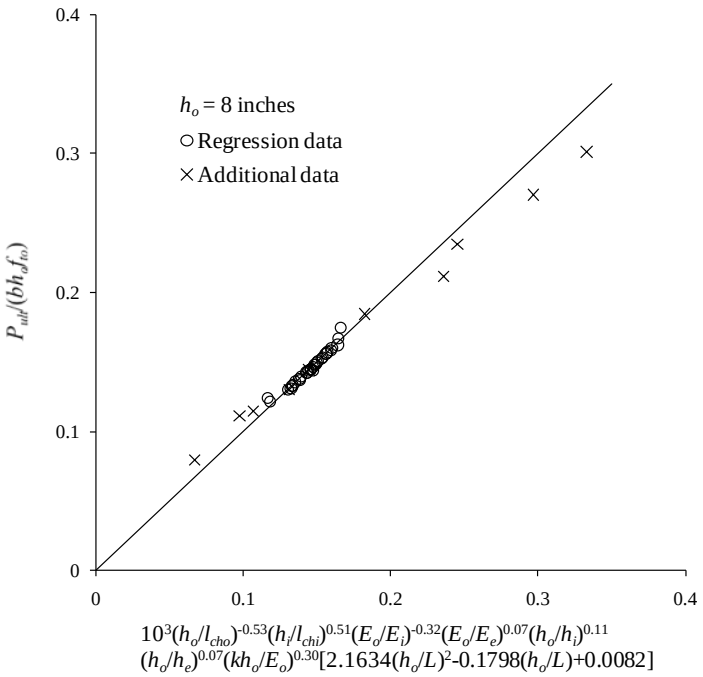

(e) h_o = 8 inches (20.32 cm)

Figure 5.3. (continued) Derived relationship between the capacity and the variables

5.3 Structural Equivalency Design

The following procedure is proposed as an illustration of how fracture mechanics can be used as the basis of UBCO design procedures.

1. For a chosen set of material and foundation properties, determine the thickness of a new single-layer pavement that is required to meet the service requirements.

2. Using Equation (4.7), determine the load capacity of the single-layer pavement.

3. Using Equation (5.1), select a combination of material properties and geometric configuration, then determine the load capacities of the UBCO systems for 4 to 8-inch-thick (10.16 to 20.32-cm-thick) overlays.

4. Select the required UBCO thickness to render the UBCO structurally equivalent to the single-layer pavement.

This procedure is illustrated for L = 20 feet (6.10 m), k = 100 pci (27.14 MPa/m), h_i = 1 inch (2.54 cm), h_e = 8 inches (20.32 cm), E_o = 4,000 ksi (27.58 GPa), E_e = 5,000 ksi (34.47 GPa), f_{to} = 400 psi (2.76 MPa), and G_{Fo} = 0.6 lb/inch (105.08 N/m). Assuming the required thickness of a new single-layer pavement is 8 inches (20.32 cm) and its material properties are the same as those of the overlay, Equation (4.7) predicts its capacity as 472 lbs (2.10 kN) (the ABAQUS simulation of this case predicts a capacity equal to 471 lbs (2.09 kN)). Assuming AC interlayer properties E_i = 500 ksi (3.45 GPa) and f_{ti} = 600 psi (4.14 MPa), Equation (5.1) predicts the load capacities for 4, 5, 6, 7, and 8-inch-thick (10.16, 12.70, 15.24, 17.78, and 20.32 cm-thick)

overlays are 384, 416, 458, 504, and 569 lbs (1.71, 1.85, 2.04, 2.24, and 2.53 kN), respectively. Therefore, the 8-inch-thick (20.32-cm-thick) single-layer pavement is equivalent to an UBCO with an overlay thickness approximately equal to 6.5 inches (16.51 cm) (by interpolation). If the properties are changed to E_i = 500 ksi (3.45 GPa) and f_{ti} = 500 psi (3.45 MPa), the required overlay thickness becomes 7.2 inches (18.29 cm), thus illustrating that the interaction between the overlay and the interlayer is significant and cannot be neglected as is done by currently used MnDOT procedures.

The examples above drive home the point that the usefulness of the fracture mechanics modeling lies in its ability to enable the designer to explore the effects of all of the material and geometric parameters on the required thickness of the overlay. If the values of the material and geometric parameters fall outside the ranges investigated in this research, the same process carried out herein can be repeated to develop similar design equations. Eventually, fracture mechanics-based design guidelines could be developed that account for all possible loadings, temperature conditions, etc. With proper choices of material properties and geometric parameters, thinner overlay thicknesses may be achieved.

5.4 Summary

Finite element model-based CZMs for UBCOs have been created by ABAQUS. With the help of dimensional analysis and DAKOTA's capability to simulate very large number of realizations, equations for the load-carrying capacities of UBCOs were derived. The equations shed light on the effects of each of the control variables and the most effective ways of improving capacity. According to the structural equivalency concept, an illustrative design procedure for UBCOs was proposed and demonstrated through several examples.

6 FIELD STUDY

6.1 Introduction

The failure analyses performed in the previous chapters are highly idealized two-dimensional approximations of the geometry and loading of UBCO structures. Two-dimensional crack configurations are expected to produce conservative results and thus the overlay thicknesses determined from these models may be conservative. However, whether this is the case for pavement systems could be determined only through more refined models and experimentation. This chapter compares the results of the two-dimensional models with observations from a field study conducted at the MnROAD research facility and summarized in Section 6.2. The comparison offers promise that overlay thicknesses can indeed be thinned-up by proper selection of material properties and geometric parameters, according to the additional information that could be provided by three-dimensional fracture mechanics simulations and experimental results.

6.2 Field Study

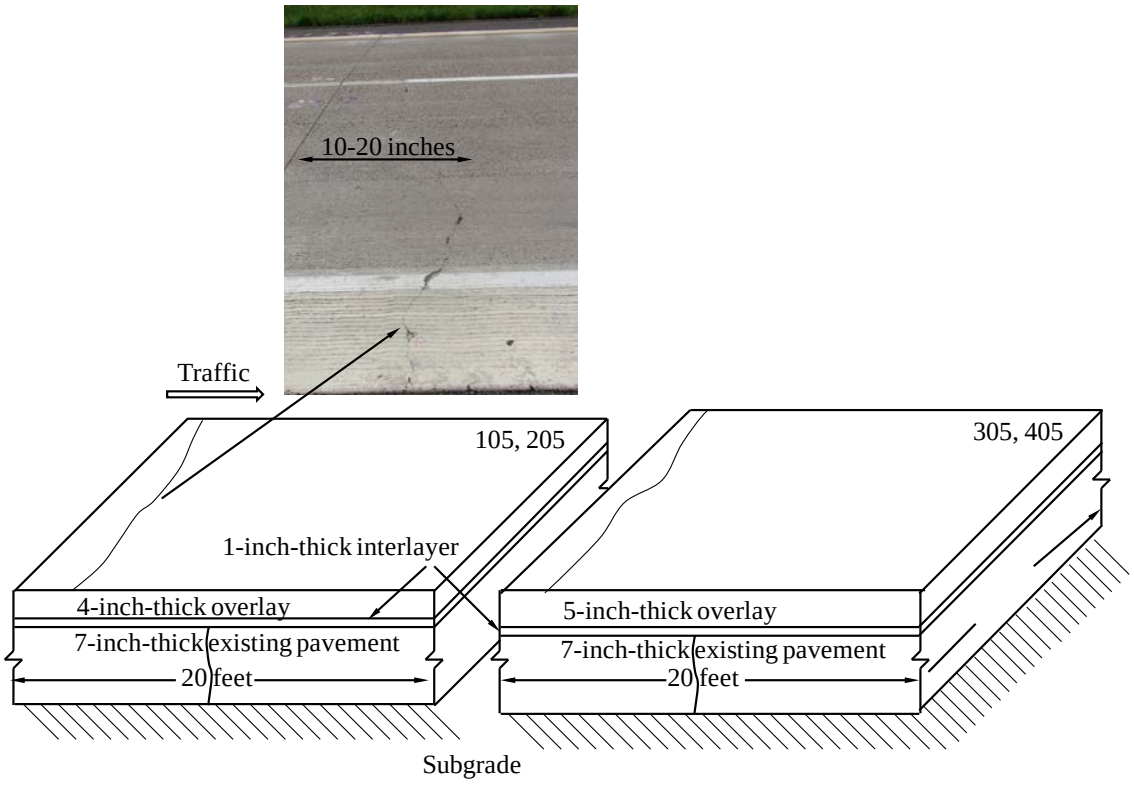

Figure 6.1. MnROAD test sections of UBCOs

In July 2010, the author observed the condition of the four UBCO test sections built in 2008 at the MnROAD test facility located parallel to westbound Interstate Highway I-94 near Albertville, Minnesota. The dimensions of the cells, numbered 105, 205, 305, and 405, are shown in the schematic in Figure 6.1; the thickness of the AC interlayer of all sections is 1 inch (2.54 cm). Also shown in the figure is an image representative of the cracking that was observed in all

sections 10-20 inches (25-50 cm) from the cell-separating joints. These cracks are not reflective. Instead they were attributed to temperature effects such as curling or warping.

Most importantly, no other cracks were observed within the overlays. This suggests that the thicknesses of the overlays are sufficient to resist the potential reflection cracking considered in this research. The developed models cannot be directly applied to interpret the MnROAD section because the material parameters of the section are not known to us. Furthermore, temperature, moisture and traffic effects are considered in the model. Further research is suggested to consider these effects in the future. Nevertheless, assuming the practical values of parameters, E_o = 4,000 ksi (27.58 GPa), E_i = 500-1,500 ksi (3.45-10.34 GPa), E_e = 5,000-9,000 ksi (34.47-62.05 GPa), f_{to} = 400-600 psi (2.76-4.14 MPa), f_{ti} = 400-600 psi (2.76-4.14 MPa), G_{Fo} = 0.6-0.9 lb/inch (105.08-157.61 N/m), G_{Fi} = 1.5-2.25 lb/inch (262.69-394.04 N/m), and k = 100 pci (27.14 MPa/m), Equations (4.7) and (5.1) state that the originally designed 7-inch-thick (17.78-cm-thick) single-layer pavement is structurally equivalent to a minimum overlay thickness of 4.8 inches (12.19 cm). Therefore the overlays 105 and 205 tested at MnROAD, even though they are almost 1 inch (2.54 cm) thinner than the lower bound suggested by the fracture mechanics-based design approach, appear to be of sufficient thickness. Additional experiments and fracture mechanics modeling, including three-dimensional simulations that represent the geometry and the loading conditions of the UBCO pavement more realistically, should provide additional insights as to whether UBCOs can be "thinned-up."

6.3 Summary

Four thin UBCO test sections conducted at the MnROAD research facility did not crack anywhere except near the poorly designed joints separating the cells. This suggests that these sections are sufficient to resist the potential reflection cracking, and that thicker overlays that would have been chosen using currently available design procedures would have been conservative. In addition, the proposed two-dimensional analysis-based design equations may also require conservative overlay thicknesses. Additional experiments and three-dimensional simulations should be considered to provide additional confidence for more cost-effective UBCO designs.

7 CONCLUSIONS AND RECOMMENDATIONS

NLFM has been applied for the first time to the analysis and design of UBCOs. The key findings of this research are summarized as follows:

- The CZM approach allows the ultimate load-carrying capacity to be expressed as a combination of power law and polynomial function of all the fundamental material and geometric parameters that describe the UBCO composite pavement system.
- The resulting design formulas can enable the pavement designer to optimize the combination of material properties and geometric dimensions to achieve a desired equivalency between the UBCO and a reference single-layer PCC pavement.
- Increasing the toughness (actually the strength since the critical crack opening displacement is assumed constant) of the interlayer and/or the overlay and decreasing the stiffness of the interlayer are effective ways of improving the load-carrying capacity of the UBCO pavement.
- The preliminary comparisons of the results with field observations suggest that currently used design procedures demand conservative overlay thicknesses.

The fracture mechanics-based design procedure for UBCOs has shown good potential for more robust designs. The field observations in Chapter 6 suggest that the overlay thickness may be "thinned-up" by additional experiments or three-dimensional modeling. Therefore, a systematic study of three-dimensional UBCOs, both experimentally and numerically, and an experimental program that can assess the accuracy of the fracture mechanics predictions are strongly recommended for future research. As the complexity of the composite system, the main difficulty would be to explore the relationship between the structural load-carrying capacity and the material properties and geometric dimensions.

REFERENCES

Adams, B. M., Bohnhoff, W. J., Dalbey, K. R., Eddy, J. P., Eldred, M. S., Gay, D. M., Haskell, K., Hough, P. D., and Swiler, L. P. (2009). *DAKOTA, a multilevel parallel object-oriented framework for design optimization, parameter estimation, uncertainty quantification, and sensitivity analysis: Version 5.0 user's manual.* Sandia Technical Report SAND2010-2183, Sandia National Laboratories, Albuquerque, NM.

American Association of State Highway and Transportation Officials (1993). *AASHTO guide for design of pavement structures*. Washington, D.C.

Applied Research Associates, Inc. and Arizona State University (2009). *Mechanistic-Empirical Pavement Design Guide (M-E PDG) Version 1.1*.

Aure, T. W. and Ioannides, A. M. (2010). "Simulation of crack propagation in concrete beams with cohesive elements in ABAQUS." *Transportation Research Record,* 2154, 12-21.

Baek, J. and Al-Qadi, I. L. (2008). "Mechanism of overlay reinforcement to retard reflective cracking under moving vehicular loading." *Pavement Cracking: Mechanisms, Modeling, Detection, Testing and Case Histories,* 563-573.

Barenblatt, G. I. (1962). "The mathematical theory of equilibrium cracks in brittle fracture." *Advances in Applied Mechanics,* 7, 55-129.

Bazant, Z. P. (2002). "Concrete fracture models: testing and practice." *Engineering Fracture Mechanics,* 69(2), 165-205.

Bazant, Z. P. and Yu, Q. (2011). "Size-effect testing of cohesive fracture parameters and nonuniqueness of work-of-fracture method." *Journal of Engineering Mechanics,* 137(8), 580-588.

Bazant, Z. P., Yu, Q., and Zi, G. (2002). "Choice of standard fracture test for concrete and its statistical evaluation." *International Journal of Fracture,* 118(4), 303-337.

Birgisson, B., Montepara, A., Romeo, E., Roncella, R., Tebaldi, G., and Roque, R. (2008). "The use of digital image correlation for accurate determination of fracture energy density in Hot Mix Asphalt (HMA)." *Pavement Cracking: Mechanisms, Modeling, Detection, Testing and Case Histories,* 811-820.

Boresi, A. P. and Schmidt, R. J. (2003). "Beams on elastic foundations." *Advanced mechanics of materials,* 6th Edition, John Wiley & Sons, Inc., Hoboken, NJ, 357-378.

Buckingham, E. (1914). "On physically similar systems; illustrations of the use of dimensional equations." *Physical Review,* 4(4), 345-376.

Cho, K. Z., Kobayashi, A. S., Hawkins, N. M., Barker, D. B., and Jeang, F. L. (1984). "Fracture process zone of concrete cracks." *Journal of Engineering Mechanics-ASCE,* 110(8), 1174-1184.

Cornelissen, H. A. W., Hordijk, D. A., and Reinhardt, H. W. (1986). "Experiments and theory for the application of fracture mechanics to normal and light weight concrete." *Fracture toughness and fracture energy of concrete,* F. H. Wittmann, ed., Elsevier, Amsterdam, The Netherlands, 565-575.

Dave, E. V., Braham, A. F., Buttlar, W. G., and Paulino, G. H. (2011). "Development of a flattened indirect tension test for asphalt concrete." *Journal of Testing and Evaluation,* 39(3).

Departments of the Army, and the Air Force (1970). *Rigid pavements for airfields other than army.* Technical Manual 5-824-3/Air Force Manual 88-6, Chapter 3, Washington, D.C.

Dugdale, D. S. (1960). "Yielding of steel sheets containing slits." *Journal of the Mechanics and Physics of Solids,* 8(2), 100-104.

Elices, M., Rocco, C., and Roselló, C. (2009). "Cohesive crack modeling of a simple concrete: experimental and numerical results." *Engineering Fracture Mechanics,* 76(10), 1398-1410.

Engstrom, G. M. (1993). *Unbonded concrete overlays Minnesota experience.* Interim Report, Minnesota Department of Transportation, St. Paul, MN.

ERES Consultants, Inc. (1999). *Evaluation of unbonded Portland cement concrete overlays.* National Cooperative Highway Research Program Report No. 415, Transportation Research Board, Washington, D.C.

ERES Consultants Division, Applied Research Associates, Inc. (2004). *Guide for mechanistic-empirical design of new and rehabilitated pavement structures.* National Cooperative Highway Research Program 1-37A, Transportation Research Board, Washington, D.C.

Fathy, A. M., Sanz, B., Sancho, J. M., and Planas, J. (2008). "Determination of the bilinear stress-crack opening curve for normal- and high-strength concrete." *Fatigue and Fracture of Engineering Material and Structures,* 31(7), 539-548.

Gaedicke Hornung, M. C. (2009). "Fracture-based method to determine the flexural load capacity of concrete slabs." Ph.D. Thesis, University of Illinois at Urbana-Champaign, Urbana, IL.

Gain, A. L., Carroll, J., Paulino, G. H., and Lambros, J. (2011). "A hybrid experimental/numerical technique to extract cohesive fracture properties for mode-I fracture of quasi-brittle materials." *International Journal of Fracture,* 169(2), 113-131.

Gopalaratnam, V. S. and Shah, S. P. (1985). "Softening response of plain concrete in direct tension." *ACI Journal*, 82(3), 310-323.

Hall, K. T., Darter, M. I., and Seiler, W. J. (1993). "Improved design of unbonded concrete overlays." *Fifth International Conference on Concrete Pavement Design and Rehabilitation,* Purdue University, West Lafayette, IN, 227-240.

Heckel, L. B. (2002). *Performance of an unbonded concrete overlay on I-74.* Physical Research Report NO. 140, Illinois Department of Transportation, Springfield, IL.

Hillerborg, A., Modeer, M., and Petersson, P.-E. (1976). "Analysis of crack formation and crack growth in concrete by means of fracture mechanics and finite elements." *Cement and Concrete Research,* 6(6), 773-782.

Hilsdorf, H. K. and Brameshuber, W. (1991). "Code-type formulation of fracture mechanics concepts for concrete." *International Journal of Fracture,* 51(1), 61-72.

Hutchinson, R. L. (1982). *Resurfacing with Portland cement concrete*. National Cooperative Highway Research Program, Synthesis of Highway Practice No. 99, Transportation Research Board, Washington, D.C.

Ioannides, A. M. (1997). "Fracture mechanics in pavement engineering: the specimen-size effect." *Transportation Research Record,* 1568, 10-16.

Ioannides, A. M. (2006). "Concrete pavement analysis: the first eighty years." *International Journal of Pavement Engineering,* 7(4), 233-249.

Ioannides, A. M., Peng, J., and Swindler Jr., J. R. (2006). "ABAQUS model for PCC slab cracking." *International Journal of Pavement Engineering,* 7(4), 311-321.

Ioannides, A. M. and Sengupta, S. (2003). "Crack propagation in Portland cement concrete beams: implications for pavement design." *Transportation Research Record,* 1853, 110-117.

Irwin, G. R. (1957). "Analysis of stresses and strains near the end of a crack traversing a plate." *Journal of Applied Mechanics,* 24(3), 361-364.

Jacobs, M. M. J., Hopman, P. C., and Molenaar, A. A. A. (1996). "Application of fracture mechanics principles to analyze cracking in asphalt concrete." *Journal of the Association of Asphalt Paving Technologists,* 65, 1-39.

Khazanovich, L. (2001). *Improved concrete overlay design parameters for airfield pavements.* Innovative Pavement Research Foundation Report DOT/FAA-01-G-002-2, Champaign, IL.

Kim, H. and Buttlar, W. G. (2009). "Finite element cohesive fracture modeling of airport pavements at low temperatures." *Cold Regions Science and Technology,* 57(2-3), 123-130.

Kim, Y. (2011). "Cohesive zone model to predict fracture in bituminous materials and asphaltic pavements: state-of-the-art review." *International Journal of Pavement Engineering,* 12(4), 343-356.

Kim, Y., Allen, D. H., and Little, D. N. (2005). "Damage-induced modeling of asphalt mixtures through computational micromechanics and cohesive zone fracture." *Journal of Materials in Civil Engineering,* 17(5), 477-484.

Kim, Y., Allen, D. H., and Little, D. N. (2007). “Computational constitutive model for predicting nonlinear viscoelastic damage and fracture failure of asphalt concrete mixtures.” *International Journal of Geomechanics,* 7(2), 102-110.

Koh, C. and Roque, R. (2010). “Use of nonuniform stress-state tests to determine fracture energy of asphalt mixtures accurately.” *Transportation Research Record,* 2181, 55-66.

Li, X. and Marasteanu, M. O. (2010). “Using semicircular bending test to evaluate low temperature fracture resistance for asphalt concrete.” *Experimental Mechanics,* 50(7), 867-876.

Marasteanu, M. O., Dai, S., Labuz, J. F., and Li, X. (2002). “Determining the low-temperature fracture toughness of asphalt mixtures.” *Transportation Research Record,* 1789, 191-199.

Miner, M. A. (1945). “Cumulative damage in fatigue.” *Journal of Applied Mechanics-ASME,* 12(3), A-159–A-164.

Minnesota Department of Transportation (1993). *Unbonded concrete overlay design procedures.* Office of Materials Research and Engineering, Pavement Engineering Section, Maplewood, MN.

Morel, S., Lespine, C., Coureau, J.-L., Planas, J., and Dourado, N. (2010). “Bilinear softening parameters and equivalent LEFM R-curve in quasibrittle failure.” *International Journal of Solids and Structures,* 47(6), 837-850.

Park, K., Paulino, G. H., and Roesler, J. R. (2008). “Determination of the kink point in the bilinear softening model for concrete.” *Engineering Fracture Mechanics,* 75(13), 3806-3818.

Park, K., Paulino, G. H., and Roesler, J. (2010). “Cohesive fracture model for functionally graded fiber reinforced concrete.” *Cement and Concrete Research,* 40(6), 956-965.

Petersson, P.-E. (1981). *Crack growth and development of fracture zones in plain concrete and similar materials.* Report TVBM-1006, Division of Building Materials, Lund Institute of Technology, Lund, Sweden.

Planas, J. and Elices, M. (1986). “Towards a measure of G_F: an analysis of experimental results.” *Fracture toughness and fracture energy of concrete,* F. H. Wittmann, ed., Elsevier, Amsterdam, The Netherlands, 381-390.

Reinhardt, H. W. (1984). “Fracture mechanics of fictitious crack propagation in concrete.” *Heron,* 29(2), 3-42.

Roesler, J., Paulino, G. H., Park, K., and Gaedicke, C. (2007). “Concrete fracture prediction using bilinear softening.” *Cement and Concrete Composites,* 29(4), 300-312.

Rokugo, K., Iwasa, M., Suzuki, T., and Koyanagi, W. (1989). “Testing methods to determine tensile strain softening curve and fracture energy of concrete.” *Fracture toughness and fracture energy: test methods for concrete and rock,* H. Mihashi, H. Takahashi, and F. H. Wittmann, eds., Balkema, Rotterdam, The Netherlands, 153-163.

Rollings, R. S. (1988). *Design of overlays for rigid airport pavements*. DOT/FAA/PM-87/19, Federal Aviation Administration, Washington, D.C.

Sangpetngam, B., Birgisson, B., and Roque, R. (2003). "Development of efficient crack growth simulator based on hot-mix asphalt fracture mechanics." *Transportation Research Record,* 1832, 105-112.

SIMULIA (2010). "ABAQUS 6.10 documentation." Providence, RI.

Smith, R. E., Palmieri, R. P., Darter, M. I., and Lytton, R. L. (1986). *Pavement overlay design procedures and assumptions-Volume I: analysis of existing procedures.* FHWA/RD-85/006, Federal Highway Administration, McLean, VA.

Song, S. H., Paulino, G. H., and Buttlar, W. G. (2006a). "A bilinear cohesive zone model tailored for fracture of asphalt concrete considering viscoelastic bulk material." *Engineering Fracture Mechanics,* 73(18), 2829-2848.

Song, S. H., Paulino, G. H., and Buttlar, W. G. (2006b). "Simulation of crack propagation in asphalt concrete using an intrinsic cohesive zone model." *Journal of Engineering Mechanics,* 132(11), 1215-1223.

Stoffels, S. (2008). *Improved overlay design parameters for concrete airfield pavements.* Innovative Pavement Research Foundation Report FAA-01-G-002-04-2, Conneaut Lake, PA.

Stoffels, S. (2010). *Improved overlay design parameters for concrete airfield pavements – SCI validation.* Innovative Pavement Research Foundation Report IPRF-01-G-002-06-3, Skokie, IL.

Tada, H., Paris, P. C., and Irwin, G. R. (1973). "*The stress analysis of cracks handbook.*" Del Research Corp., St. Louis, MO.

Tayabji, S. D. and Okamoto, P. A. (1985). "Thickness design of concrete resurfacing." *Third International Conference on Concrete Pavement Design and Rehabilitation,* Purdue University, West Lafayette, IN, 367-379.

Veverka, V. (1986). "The Belgian road research center's design procedure for concrete pavements." Brussels, Belgium.

Wagoner, M. P., Buttlar, W. G., Paulino, G. H., and Blankenshi, P. (2005). "Investigation of the fracture resistance of hot-mix asphalt concrete using a disk-shaped compact tension test." *Transportation Research Record,* 1929, 183-192.

Westergaard, H. M. (1947). "New formulas for stresses in concrete pavements of airfields." *American Society of Civil Engineers,* 73(5), 687-701.

Wittmann, F. H., Rokugo, K., Brühwiler, E., Mihashi, H., and Simonin, P. (1988). "Fracture energy and strain softening of concrete as determined by means of compact tension specimens." *Materials and Structures,* 21(1), 21-32.

APPENDIX A: MNDOT UBCO DESIGN PROCEDURE

The MnDOT UBCO design procedure consists of the following:

(1) Existing pavement evaluation, including pavement condition survey, such as the type, extent and severity of the distresses, and falling weight deflectometer (FWD) load testing, if possible, to determine the pavement's elastic modulus, the modulus of subgrade reaction, etc.

(2) Traffic analysis. In accordance with current policy, UBCO thickness designs are based on anticipated cumulative 30-year design lane rigid Equivalent Single Axle Loads ($CESAL_{30}$).

(3) Subgrade reaction (k) determination. It can be calculated using the following equation from the design R-value (average minus one standard deviation): $k = 1.17 + 63\sqrt{R}$.

(4) New PCC pavement thickness design. Use PAVE program (based on 1972 AASHTO, revised 1981) with the following parameters: design R-value, 30-year design lane traffic $\times$ 0.93 (modified for frozen subgrade effect), modulus of rupture (M_r = 500 psi), modulus of elasticity (E = 4,200 ksi), J-factor (J = 2.6 for 27-foot wide pavement and J = 3.2 for 24-foot wide pavement), etc.

(5) Overlay thickness design.

a. COE procedure. Use Equation (2.1). h_n is from PAVE program (do not round) and C is selected from step (1).

b. PCA procedure. Use design charts in Figure 2.2 to determine the required overlay thickness.

c. Average the results of above two procedures. Round the average result in accordance with the following rounding procedures: x.0 to x.1 round to x.0, x.2 to x.6 round to x.5, and x.7 to x.9 round to (x+1).0. Use this value for the UBCO design thickness. However, the minimum design thickness listed in Table 2.1 should be followed.

To demonstrate the procedure, a design example is presented as follows.

(1) Design information:

a. Existing roadway: four-lane divided highway, 22 years old.

b. Existing pavement: 9.0-inch Jointed Reinforced Concrete Pavement (JRCP), 5.0-inch granular subbase, 40-foot joint spacing, 24-foot wide, dowelled joints.

c. Roadbed soils: clay loam, design R-value = 15, k = 240 psi.

d. Major distresses: mid-panel cracks, joint deterioration (severely D-cracked), PSR = 2.7, PQI = 2.6.

e. Traffic: $CESAL_{30}$ = 24,698,000.

f. Proposed design: 15-foot joint spacing, all joints dowelled, 27-foot wide pavement.

(2) New pavement design: design R-value = 15, k = 240 psi, J = 2.6, M_r = 500 psi, E = 4,200 ksi, P_t = 2.5, $CESAL_{30}$ = 24,698,000 $\times$ 0.93 = 22,969,000.

PAVE program results in a new full-depth pavement thickness of 9.7 inches - h_n.

(3) Overlay thickness design:

a. COE procedure: $h_o = \sqrt{h_n^2 - Ch_e^2} = \sqrt{9.7^2 - 0.5(9.0)^2}$ = 7.3 inches.

b. PCA procedure: according to Figure 2.2 Case (a), h_o = 8.2 inches.

c. Average of results: (7.3 + 8.2)/2 = 7.8 inches.

Design overlay 8.0 inches thick.

APPENDIX B: COHESIVE ELEMENTS IN ABAQUS

In 2005, ABAQUS Version 6.5 included for the first time "a library of cohesive elements to model the behavior of adhesive joints, interfaces in composites, and other situations where the integrity and strength of interfaces may be of interest (SIMULIA 2010)." The mechanical constitutive behavior of the cohesive elements can be defined by using a constitutive model specified directly in terms of traction versus separation as shown in Figure B.1. In the range before the softening part of the curve, a constant element stiffness (penalty stiffness) K is assumed. ABAQUS recommends a value of $K = E / T$, where E is the Young's modulus of the bulk material and T is the initial thickness of the cohesive elements. As Aure and Ioannides (2010) pointed out, the selections of K and T are largely based on prior experience using the program, yet the selections can influence the solution convergence significantly. As refining the cohesive elements (the thickness T approaches zero), K approaches infinity. A very large K results in ill-conditioning of the element operator that is detrimental to numerical stability, and therefore results in lack of convergence (SIMULIA 2010). On the other hand, low K values result in low initial stiffness of structural responses and low load-carrying capacity. As a result, Gaedicke Hornung (2009) recommended successive trials to obtain K as high as possible. However, this process is trial-based and is required to be repeated for different shapes and values of softening curves.

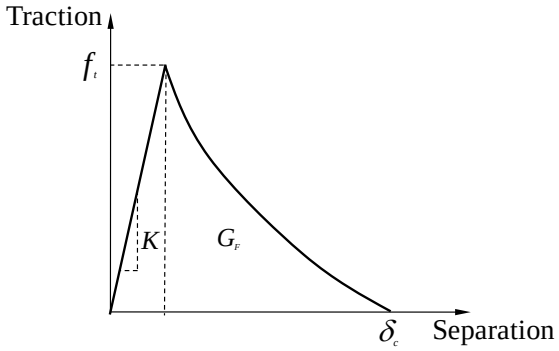

Figure B.1. Constitutive traction-separation relationship

For example, Figure B.2 plots the load versus the crack mouth opening displacement (CMOD) for the notched concrete beam under three-point bending studied in Section 3.3. The material constants are E = 4,647 ksi and ν = 0.15. First, the linear softening traction-separation law with f_t = 602 psi and G_F = 0.95 lb/inch was assumed. The initial slope and the maximum load decrease with decreasing cohesive element stiffness. Then, the bilinear cohesive law adopted in Section 3.3 was employed. In ABAQUS, the cohesive law can be input by only two default shapes, linear and exponential, and one arbitrary shape in tabular form. Therefore, the tabular form is required to input the bilinear cohesive law. The tabular form is expressed as a combination of a scalar damage variable and the crack opening displacement. The damage variable varies from 0 to 1 when the critical crack opening displacement is reached.

Before inputting the bilinear cohesive law, the results from the default linear shape are to be compared to those from a two-point input tabular form (0,0) and (1, $\delta_c - \frac{f_t}{K}$), which produces the same tensile strength, fracture energy, and critical crack opening displacement, to check the simulation consistency. Other input parameters and the discretized mesh are the same. However,

the tabular form cannot capture the softening behavior of the cohesive elements and output linear elastic behavior.

Moreover, as shown in Figure B.2, the bilinear cohesive law with high values of K cannot capture the softening behavior of the cohesive elements, and the bilinear cohesive law with low values of K predicts the structural response far away from the experimental results. This unreliability of the cohesive element simulation resulted in abandoning the approach in this research in favor of the concrete damaged plasticity model available in ABAQUS that does not involve the penalty stiffness K.

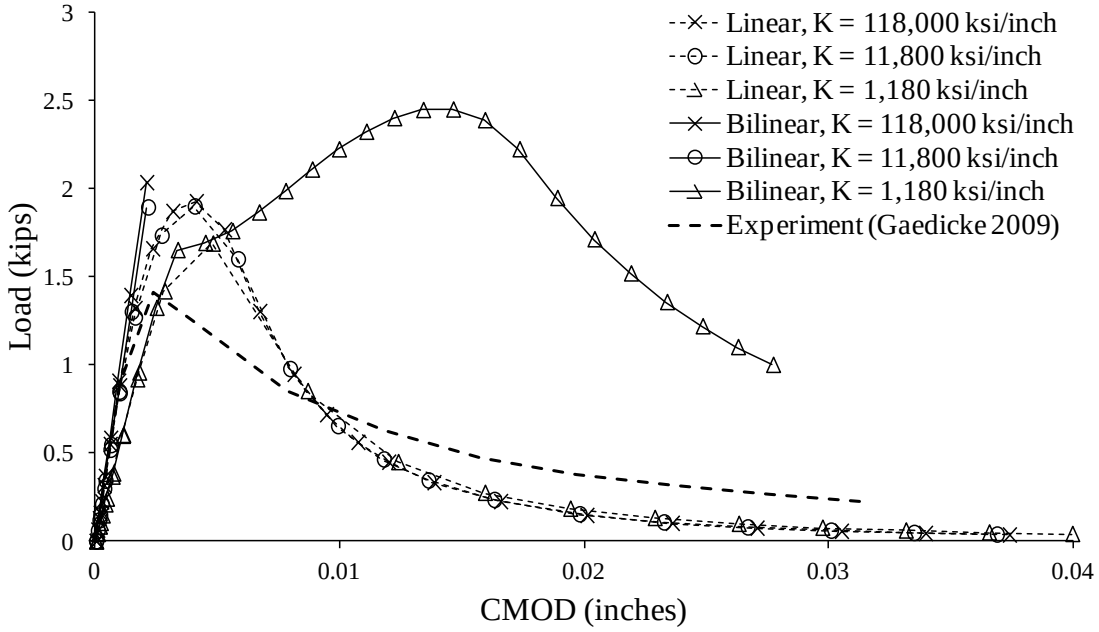

Figure B.2. Influence of penalty stiffness

APPENDIX C: BEAMS ON ELASTIC FOUNDATIONS

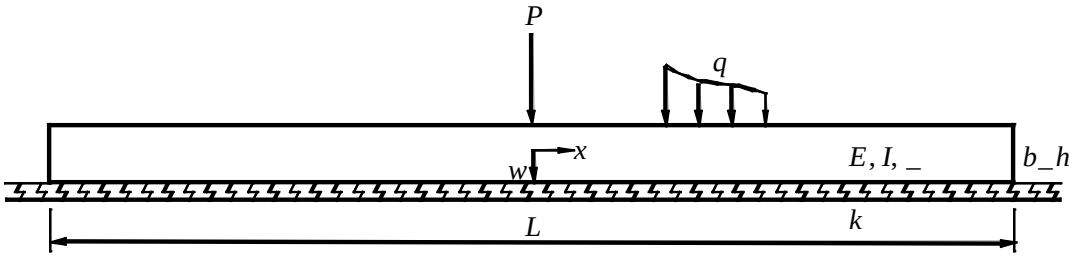

Figure C.1. A finite-length beam on an elastic foundation

The governing differential equation of a finite-length beam resting on an elastic foundation and subjected to transverse loads, as shown in Figure C.1, can be derived from a free body diagram of a differential beam element. The equation is written as

$$EI\frac{d^4w}{dx^4}+kw=q \tag{C.1}$$

where E is the Young's modulus, I is the second moment of area, k is the foundation stiffness, and q is the transverse load. By introducing a parameter β defined as

$$\beta=\sqrt[4]{\frac{k}{4EI}} \tag{C.2}$$

The general solution of the governing equation can be expressed as

$$w=e^{\beta x}\left(C_1\sin\beta x+C_2\cos\beta x\right)+e^{-\beta x}\left(C_3\sin\beta x+C_4\cos\beta x\right) \tag{C.3}$$

where C_1, C_2, C_3, and C_4 are constants.

If the beam is subjected to a concentrated load P at the center, the boundary conditions of the beam are: at $x=0$, the slope $\theta=0$ and the shear force $V=-\frac{P}{2}$; at $x=\frac{L}{2}$, the bending moment $M=0$ and the shear force $V=0$. Substituting Equation (C.3) into

$$\theta=\frac{dw}{dx},\ M=-EI\frac{d^2w}{dx^2},\ V=\frac{dM}{dx} \tag{C.4}$$

and applying the boundary conditions, four linear equations for the unknowns C_1, C_2, C_3, and C_4 are obtained. Solving the linear equations, the four constants are solved:

$$C_1=\frac{P\left(-1+e^{\beta L}\sin\beta L+e^{\beta L}\cos\beta L\right)}{16EI\beta^3e^{\beta L}(\sinh\beta L+\sin\beta L)}$$

$$C_2=\frac{P\left(1+2e^{\beta L}-e^{\beta L}\sin\beta L+e^{\beta L}\cos\beta L\right)}{16EI\beta^3e^{\beta L}(\sinh\beta L+\sin\beta L)}$$

$$C_3 = \frac{Pe^{\beta L}\left(e^{\beta L} + \sin\beta L - \cos\beta L\right)}{16EI\beta^3 e^{\beta L}(\sinh\beta L + \sin\beta L)}$$

$$C_4 = \frac{Pe^{\beta L}\left(2 + e^{\beta L} + \sin\beta L + \cos\beta L\right)}{16EI\beta^3 e^{\beta L}(\sinh\beta L + \sin\beta L)} \tag{C.5}$$

Substituting Equation (C.5) into Equation (C.4) at $x = 0$, the bending moment at the center of the beam is obtained as

$$M\left(x = 0\right) = \frac{P}{4\beta}\frac{\cosh\beta L - \cos\beta L}{\sinh\beta L + \sin\beta L} \tag{C.6}$$

Note that if the beam has a unit width $b = 1$, the introduced parameter β is related to the radius of relative stiffness $l = \sqrt[4]{\frac{Eh^3}{12\left(1-\nu^2\right)k}}$ by

$$\beta = \frac{1}{l\sqrt[4]{4\left(1-\nu^2\right)}} \tag{C.7}$$

Therefore, the bending moment at the center of the beam is

$$M(x = 0) = \frac{\sqrt[4]{4\left(1-\nu^2\right)}}{4} Pl\Phi \tag{C.8}$$

where

$$\Phi = \frac{\cosh\left[\frac{1}{\sqrt[4]{4\left(1-\nu^2\right)}}\frac{L}{l}\right] - \cos\left[\frac{1}{\sqrt[4]{4\left(1-\nu^2\right)}}\frac{L}{l}\right]}{\sinh\left[\frac{1}{\sqrt[4]{4\left(1-\nu^2\right)}}\frac{L}{l}\right] + \sin\left[\frac{1}{\sqrt[4]{4\left(1-\nu^2\right)}}\frac{L}{l}\right]} \tag{C.9}$$

APPENDIX D: DAKOTA

The ABAQUS model communicates with DAKOTA through the ABAQUS Scripting Interface scripts, i.e. Python scripts. The scripts can create and modify an ABAQUS model, submit the model for analysis, and read results from the output database. A brief description of the process to implement is summarized as follows.

(1) Create the ABAQUS pavement model (pavement.cae) with arbitrary values for the input parameters.

(2) Create a DAKOTA input file (pavement.in) to generate values of the input parameters for the parameter study.

(3) Run a Python script (abaqusinput.py) to change the values of the input parameters in the ABAQUS model, and successively, generate the ABAQUS input file (pavement.inp).

(4) Submit the ABAQUS input file via a batch file (driver.bat).

(5) After the computation is done, read output displacements and reaction forces from the output database via a Python script (abaqusoutput.py), and postprocess the data, including load-displacement curves and maximum load.

The above files for an illustrative example are attached as follows for demonstration.

(1) DAKOTA input file – pavement.in

```
strategy,
        single_method
          graphics, tabular_graphics_data

method,
        multidim_parameter_study
          partitions = 1 2 3 2

model,
        single

variables,
        continuous_design = 4
          lower_bounds =        3e6      0.15      450       100
          upper_bounds =        4e6      0.25      600       300
          descriptors = 'youngs'  'poissons'  'tensile'  'foundation'

interface,
        system
          analysis_driver = 'driver.bat'
          parameters_file = 'params.in'
          results_file = 'results.out'

responses,
        num_objective_functions = 1
        no_gradients
```

no_hessians

(2) Python script to change parameters and generate ABAQUS input file – abaqusinput.py

```
# import modules
import sys
import os

# append ABAQUS Python path
sys.path.append('C:\SIMULIA\Abaqus\6.9-1\Python')

# import ABAQUS modules
from abaqus import *
from abaqusConstants import *

# access DAKOTA params.in
f1 = sys.argv[-1]                  # params.in
f1_pointer = open(f1, 'r')         # open params.in
f1data = f1_pointer.readlines()    # read all lines in params.in
i = 1                              # initialization
for row in f1data:
   if i == 2:
      X = row.split()
      youngs = float(X[0])       # row 2 = Young's modulus
   if i == 3:
      X = row.split()
      poissons = float(X[0])     # row 3 = Poisson's ratio
   if i == 4:
      X = row.split()
      tensile = float(X[0])      # row 4 = tensile strength
   if i == 5:
      X = row.split()
      foundation = float(X[0])   # row 5 = foundation stiffness
   i = i+1

# close params.in
f1_pointer.close()

# open ABAQUS model database and change parameters
openMdb('pavement.cae')

# Material-1 and Material-2's Young's modulus and Poisson's ratio
mdb.models['Model-1'].materials['Material-1'].elastic.setValues(table=((youngs, poissons), ))
mdb.models['Model-1'].materials['Material-2'].elastic.setValues(table=((youngs, poissons), ))
# Material-2's concrete damaged plasticity
```

```
mdb.models['Model-1'].materials['Material-
2'].concreteDamagedPlasticity.concreteTensionStiffening.setValues(table=((tensile,          0.0),
(tensile/4, 0.001), (tensile/100, 0.008)))
# Foundation stiffness
a = mdb.models['Model-1'].rootAssembly
region=a.surfaces['Surf-1']
mdb.models['Model-1'].interactions['Int-1'].setValues(surface=region, stiffness=foundation)

# generate ABAQUS input file pavement.inp
mdb.jobs['pavement'].writeInput(consistencyChecking=OFF)

# close ABAQUS model database
mdb.close()

# END - ABAQUS input file with the parameters from DAKOTA has been generated.
```

(3) Partial ABAQUS input file – pavement.inp

```
*Heading
** Job name: pavement Model name: Model-1
** Generated by: Abaqus/CAE 6.9-1
*Preprint, echo=NO, model=NO, history=NO, contact=NO
……
**
** MATERIALS
**
*Material, name=Material-1
*Elastic
 3e+06, 0.15
*Material, name=Material-2
*Elastic
 3e+06, 0.15
*Concrete Damaged Plasticity
30.,0.,0.,0.,0.
*Concrete Compression Hardening
2900.,0.
*Concrete Tension Stiffening, type=DISPLACEMENT
450.,    0.
112.5, 0.001
  4.5, 0.008
*Concrete Tension Damage, type=DISPLACEMENT
  0.,    0.
 0.9, 0.008
**
** INTERACTIONS
**
** Interaction: Int-1
```

```
*Foundation
_Surf-1_S4, F4, 100.
_Surf-1_S2, F2, 100.
_Surf-1_S1, F1, 100.
_Surf-1_S3, F3, 100.
……
```

(4) Batch file – driver.bat

```
@echo off
(
abaqus cae noGUI=abaqusinput.py -- %1
abaqus job=pavement interactive
abaqus python abaqusoutput.py
copy dummy.out %2%
)
```

(5) Python script to read outputs – abaqusoutput.py

```
# import modules
import sys
import os

# append ABAQUS Python path
sys.path.append('C:\SIMULIA\Abaqus\6.9-1\Python')

# import ABAQUS modules
from abaqusConstants import *
from odbAccess import *

# open output database
odb = openOdb('pavement.odb')

# define output step
dframe = odb.steps['Step-1']

# get displacements and reaction forces in Y-direction
u2Data = dframe.historyRegions['Node PART-1-1.2'].historyOutputs['U2'].data
RFData1 = dframe.historyRegions['Node PART-1-1.2'].historyOutputs['RF2'].data
RFData2 = dframe.historyRegions['Node PART-1-1.3'].historyOutputs['RF2'].data

# open output file
f1 = open ('dummy.out', 'a')

# write displacement and reaction force data
for i in range(len(u2Data)):
    RFData = RFData1[i][1] + RFData2[i][1]
```

```
    print >> f1, -u2Data[i][1], -RFData

# close output file and database
f1.close()
odb.close()

# delete all extra files for the next run
os.remove('pavement.odb')
os.remove('pavement.com')
os.remove('pavement.dat')
os.remove('pavement.msg')
os.remove('pavement.prt')
os.remove('pavement.sta')

# END - ABAQUS output database has been accessed and displacement and reaction force values have been returned to dummy.out.
```

APPENDIX E: SIMULATION RESULTS

h_o = 4 inches, E_o = 4,000 ksi

L (inches)	k (psi/inch)	h_i (inches)	h_e (inches)	E_i (ksi)	E_e (ksi)	f_{to} (psi)	f_{ti} (psi)	P_{ult} (lbs)
144	200	1	9	1,000	7,000	500	500	345.298
168	200	1	9	1,000	7,000	500	500	367.966
192	200	1	9	1,000	7,000	500	500	401.462
216	200	1	9	1,000	7,000	500	500	441.998
240	200	1	9	1,000	7,000	500	500	480.119
192	100	1	9	1,000	7,000	500	500	280.424
192	150	1	9	1,000	7,000	500	500	343.487
192	250	1	9	1,000	7,000	500	500	453.973
192	300	1	9	1,000	7,000	500	500	500.819
192	200	0.5	9	1,000	7,000	500	1,000	446.988
192	200	1.5	9	1,000	7,000	500	333	382.453
192	200	2	9	1,000	7,000	500	250	375.550
192	200	1	6	1,000	7,000	500	500	404.847
192	200	1	12	1,000	7,000	500	500	403.190
192	200	1	9	500	7,000	500	250	349.101
192	200	1	9	750	7,000	500	375	371.073
192	200	1	9	1,250	7,000	500	625	437.768
192	200	1	9	1,500	7,000	500	750	477.609
192	200	1	9	1,000	5,000	500	500	408.882
192	200	1	9	1,000	6,000	500	500	403.680
192	200	1	9	1,000	8,000	500	500	400.904
192	200	1	9	1,000	9,000	500	500	395.324
192	200	1	9	1,000	7,000	400	500	366.819
192	200	1	9	1,000	7,000	450	500	386.454
192	200	1	9	1,000	7,000	550	500	417.055
192	200	1	9	1,000	7,000	600	500	432.165
192	200	1	9	1,000	7,000	500	400	367.432
192	200	1	9	1,000	7,000	500	450	382.327
192	200	1	9	1,000	7,000	500	550	423.759
192	200	1	9	1,000	7,000	500	600	444.724
Additional data								
144	100	0.5	12	1,500	9,000	600	400	210.514
168	100	1	12	1,500	8,000	500	500	253.552
168	200	1	9	1,500	9,000	600	400	345.080
192	200	1	9	1,000	7,000	500	500	401.462
192	300	1	9	1,000	8,000	500	500	510.860
192	300	1	9	1,000	6,000	400	600	518.877
216	200	1.5	9	500	6,000	400	600	590.906
240	300	1	9	500	5,000	400	600	677.087
240	300	1.5	6	500	5,000	400	600	738.697
240	300	2	6	500	5,000	400	600	850.949

h_o = 5 inches, E_o = 4,000 ksi

L (inches)	k (psi/inch)	h_i (inches)	h_e (inches)	E_i (ksi)	E_e (ksi)	f_{to} (psi)	f_{ti} (psi)	P_{ult} (lbs)
144	200	1	9	1,000	7,000	500	500	400.243
168	200	1	9	1,000	7,000	500	500	408.140
192	200	1	9	1,000	7,000	500	500	431.778
216	200	1	9	1,000	7,000	500	500	462.021
240	200	1	9	1,000	7,000	500	500	497.742
192	100	1	9	1,000	7,000	500	500	320.159
192	150	1	9	1,000	7,000	500	500	375.943
192	250	1	9	1,000	7,000	500	500	484.258
192	300	1	9	1,000	7,000	500	500	534.301
192	200	0.5	9	1,000	7,000	500	1,000	472.848
192	200	1.5	9	1,000	7,000	500	333	414.486
192	200	2	9	1,000	7,000	500	250	395.660
192	200	1	6	1,000	7,000	500	500	437.327
192	200	1	12	1,000	7,000	500	500	425.888
192	200	1	9	500	7,000	500	250	371.213
192	200	1	9	750	7,000	500	375	396.861
192	200	1	9	1,250	7,000	500	625	473.511
192	200	1	9	1,500	7,000	500	750	521.175
192	200	1	9	1,000	5,000	500	500	440.563
192	200	1	9	1,000	6,000	500	500	435.866
192	200	1	9	1,000	8,000	500	500	428.182
192	200	1	9	1,000	9,000	500	500	425.549
192	200	1	9	1,000	7,000	400	500	397.438
192	200	1	9	1,000	7,000	450	500	414.844
192	200	1	9	1,000	7,000	550	500	448.814
192	200	1	9	1,000	7,000	600	500	463.935
192	200	1	9	1,000	7,000	500	400	393.605
192	200	1	9	1,000	7,000	500	450	411.288
192	200	1	9	1,000	7,000	500	550	454.709
192	200	1	9	1,000	7,000	500	600	479.855
Additional data								
144	100	0.5	12	1,500	9,000	600	400	260.469
144	100	1	12	1,500	8,000	600	500	340.762
168	200	1	9	1,500	9,000	600	400	384.503
192	200	1	9	1,000	7,000	500	500	431.778
192	300	1	9	1,000	6,000	500	500	535.650
192	300	1	9	1,000	6,000	400	600	551.530
216	200	1.5	9	500	6,000	400	600	589.341
240	300	1	9	500	5,000	400	600	678.845
240	300	1.5	6	500	5,000	400	600	765.504
240	300	2	6	500	5,000	400	600	872.941

h_o = 6 inches, E_o = 4,000 ksi

L (inches)	k (psi/inch)	h_i (inches)	h_e (inches)	E_i (ksi)	E_e (ksi)	f_{to} (psi)	f_{ti} (psi)	P_{ult} (lbs)
144	200	1	9	1,000	7,000	500	500	467.716
168	200	1	9	1,000	7,000	500	500	461.102
192	200	1	9	1,000	7,000	500	500	470.650
216	200	1	9	1,000	7,000	500	500	496.346
240	200	1	9	1,000	7,000	500	500	524.803
192	100	1	9	1,000	7,000	500	500	366.349
192	150	1	9	1,000	7,000	500	500	420.035
192	250	1	9	1,000	7,000	500	500	519.925
192	300	1	9	1,000	7,000	500	500	566.319
192	200	0.5	9	1,000	7,000	500	1,000	517.530
192	200	1.5	9	1,000	7,000	500	333	450.093
192	200	2	9	1,000	7,000	500	250	441.360
192	200	1	6	1,000	7,000	500	500	480.545
192	200	1	12	1,000	7,000	500	500	465.137
192	200	1	9	500	7,000	500	250	406.022
192	200	1	9	750	7,000	500	375	434.782
192	200	1	9	1,250	7,000	500	625	518.908
192	200	1	9	1,500	7,000	500	750	571.102
192	200	1	9	1,000	5,000	500	500	482.951
192	200	1	9	1,000	6,000	500	500	477.239
192	200	1	9	1,000	8,000	500	500	466.405
192	200	1	9	1,000	9,000	500	500	465.873
192	200	1	9	1,000	7,000	400	500	433.483
192	200	1	9	1,000	7,000	450	500	452.702
192	200	1	9	1,000	7,000	550	500	492.102
192	200	1	9	1,000	7,000	600	500	511.202
192	200	1	9	1,000	7,000	500	400	429.809
192	200	1	9	1,000	7,000	500	450	448.270
192	200	1	9	1,000	7,000	500	550	497.759
192	200	1	9	1,000	7,000	500	600	524.492
Additional data								
168	100	0.5	12	1,500	9,000	600	400	305.891
144	100	1	12	1,500	8,000	600	500	415.752
144	200	1	9	1,500	9,000	600	400	427.278
192	200	1	9	1,000	7,000	500	500	470.650
192	300	1	9	1,000	6,000	500	500	575.187
192	300	1	9	1,000	6,000	400	600	584.884
192	300	1	9	500	5,000	400	600	604.087
240	300	1	9	500	5,000	400	600	692.550
240	300	1.5	6	500	5,000	400	600	795.696
240	300	2	6	500	5,000	400	600	900.353

h_o = 7 inches, E_o = 4,000 ksi

L (inches)	k (psi/inch)	h_i (inches)	h_e (inches)	E_i (ksi)	E_e (ksi)	f_{to} (psi)	f_{ti} (psi)	P_{ult} (lbs)
144	200	1	9	1,000	7,000	500	500	545.794
168	200	1	9	1,000	7,000	500	500	522.534
192	200	1	9	1,000	7,000	500	500	522.366
216	200	1	9	1,000	7,000	500	500	535.938
240	200	1	9	1,000	7,000	500	500	559.612
192	100	1	9	1,000	7,000	500	500	424.566
192	150	1	9	1,000	7,000	500	500	474.235
192	250	1	9	1,000	7,000	500	500	568.441
192	300	1	9	1,000	7,000	500	500	613.998
192	200	0.5	9	1,000	7,000	500	1,000	566.679
192	200	1.5	9	1,000	7,000	500	333	502.412
192	200	2	9	1,000	7,000	500	250	489.143
192	200	1	6	1,000	7,000	500	500	539.090
192	200	1	12	1,000	7,000	500	500	513.666
192	200	1	9	500	7,000	500	250	448.366
192	200	1	9	750	7,000	500	375	479.517
192	200	1	9	1,250	7,000	500	625	573.232
192	200	1	9	1,500	7,000	500	750	631.327
192	200	1	9	1,000	5,000	500	500	533.744
192	200	1	9	1,000	6,000	500	500	528.101
192	200	1	9	1,000	8,000	500	500	517.594
192	200	1	9	1,000	9,000	500	500	513.819
192	200	1	9	1,000	7,000	400	500	476.568
192	200	1	9	1,000	7,000	450	500	499.385
192	200	1	9	1,000	7,000	550	500	542.715
192	200	1	9	1,000	7,000	600	500	563.755
192	200	1	9	1,000	7,000	500	400	474.782
192	200	1	9	1,000	7,000	500	450	497.916
192	200	1	9	1,000	7,000	500	550	543.371
192	200	1	9	1,000	7,000	500	600	578.957
Additional data								
168	100	0.5	12	1,500	9,000	600	400	364.819
168	100	1	12	1,500	9,000	500	400	384.644
144	200	1	9	1,500	9,000	600	400	516.851
192	200	1	9	1,000	7,000	500	500	522.366
192	300	1	9	1,000	6,000	500	500	619.964
192	300	1	9	1,000	6,000	400	600	631.191
216	200	1.5	9	500	5,000	400	600	650.400
240	300	1	9	500	5,000	400	600	718.234
240	300	1.5	6	500	5,000	400	600	828.619
240	300	2	6	500	5,000	400	600	931.280

h_o = 8 inches, E_o = 4,000 ksi

L (inches)	k (psi/inch)	h_i (inches)	h_e (inches)	E_i (ksi)	E_e (ksi)	f_{to} (psi)	f_{ti} (psi)	P_{ult} (lbs)
144	200	1	9	1,000	7,000	500	500	632.548
168	200	1	9	1,000	7,000	500	500	592.865
192	200	1	9	1,000	7,000	500	500	579.839
216	200	1	9	1,000	7,000	500	500	576.068
240	200	1	9	1,000	7,000	500	500	602.525
192	100	1	9	1,000	7,000	500	500	485.459
192	150	1	9	1,000	7,000	500	500	532.507
192	250	1	9	1,000	7,000	500	500	624.155
192	300	1	9	1,000	7,000	500	500	667.786
192	200	0.5	9	1,000	7,000	500	1,000	627.991
192	200	1.5	9	1,000	7,000	500	333	557.764
192	200	2	9	1,000	7,000	500	250	542.481
192	200	1	6	1,000	7,000	500	500	597.901
192	200	1	12	1,000	7,000	500	500	570.603
192	200	1	9	500	7,000	500	250	497.532
192	200	1	9	750	7,000	500	375	531.556
192	200	1	9	1,250	7,000	500	625	625.028
192	200	1	9	1,500	7,000	500	750	699.337
192	200	1	9	1,000	5,000	500	500	593.444
192	200	1	9	1,000	6,000	500	500	586.479
192	200	1	9	1,000	8,000	500	500	574.740
192	200	1	9	1,000	9,000	500	500	570.287
192	200	1	9	1,000	7,000	400	500	519.502
192	200	1	9	1,000	7,000	450	500	551.753
192	200	1	9	1,000	7,000	550	500	602.736
192	200	1	9	1,000	7,000	600	500	628.833
192	200	1	9	1,000	7,000	500	400	520.693
192	200	1	9	1,000	7,000	500	450	551.968
192	200	1	9	1,000	7,000	500	550	610.048
192	200	1	9	1,000	7,000	500	600	641.400
Additional data								
240	100	0.5	12	1,500	9,000	600	400	381.402
168	100	1	12	1,500	9,000	600	500	533.915
192	200	1	10	1,500	9,000	600	400	550.155
192	200	1	9	1,000	8,000	600	500	624.721
192	200	1	10	1,000	7,000	500	500	576.459
192	300	1	9	1,000	6,000	500	600	738.054
192	300	1	10	500	5,000	400	600	677.613
240	300	1	9	500	5,000	400	600	750.423
240	300	1.5	6	500	5,000	400	600	864.631
240	300	2	6	500	5,000	400	600	963.740